1 Shapes of magnetically controlled electron density structures in the dayside Martian ionosphere

2 C. Diéval[1], A. J. Kopf[2] and J. A. Wild[1].

3 [1]Department of Physics, Lancaster University, Lancaster, UK.

4 [2]Department of Physics and Astronomy, University of Iowa, Iowa City, IA, USA.

5 Corresponding author: cdieval05@gmail.com

6 Key points:

7 1. MARSIS AIS/Mars Express shows magnetically controlled density structures in the

8   dayside Martian ionosphere.

9 2. Time series of electron density profiles corrected for dispersion are used to find the shape

10   of 48 structures.

11 3. The majority of these structures are bulges, and a few are of other simple shapes: dip,

12   downhill slope and uphill slope.

13

14 Abstract:

15   Non-horizontal localized electron density structures associated with regions of near radial

16 crustal magnetic fields are routinely detected via radar oblique echoes on the dayside of Mars

17 with the ionospheric sounding mode of the MARSIS radar onboard Mars Express. Previous

18 studies mostly investigated these structures at a fixed plasma frequency and assumed that the

19 larger apparent altitude of the structures compared to the normal surrounding ionosphere implied

20 that they are bulges. However, the signal is subjected to dispersion when it propagates through

the plasma, so interpretations based on the apparent altitude should be treated with caution. We go further by investigating the frequency dependence (i.e. the altitude dependence) of the shape of 48 density structure events, using time series of MARSIS electron density profiles (EDPs) corrected for signal dispersion. Four possible simplest shapes are detected in these time series, which can give oblique echoes: bulges, dips, downhill slopes and uphill slopes. The altitude differences between the density structures and their edges are, in absolute value, larger at low frequency (high altitude) than at high frequency (low altitude), going from a few tens of km to a few km as frequency increases. Bulges dominate in numbers in most of the frequency range. Finally, the geographical extension of the density structures covers a wide range of crustal magnetic fields orientations, with near-vertical fields toward their center and near horizontal fields toward their edges, as expected. Transport processes are suggested to be a key driver for these density structures.

1) Introduction

The Martian upper atmosphere is not currently protected by a global magnetic dipole, and is therefore exposed to erosion by the incoming supersonic solar wind. An induced magnetosphere arises from the interaction between the conductive ionospheric obstacle and the solar wind plasma with its embedded interplanetary magnetic field (IMF) (e.g. Nagy et al., 2004). In addition, localized crustal magnetic fields (e.g. Acuña et al., 1999), remnants of a past Martian dynamo, are able to stand off the solar wind and locally control the magnetic topology at low altitudes in the forms of magnetic arcades with both footpoints anchored in the planetary crust (closed field lines), while in other areas the IMF is free to reach lower altitudes, imposing a

43   mostly horizontal induced magnetic field on the dayside (e.g. Brain et al., 2003). The magnetic

44   anomalies form mini-magnetospheres which rotate with the planet, locally regulating

45   atmospheric loss (e.g. Ramstad et al., 2016).

46   The Mars Advanced Radar for Subsurface and Ionospheric Sounding (MARSIS)

47   experiment (Picardi et al., 2004) is part of the payload onboard the Mars Express (MEX) orbiter.

48   MEX orbit has period 7.5 h and inclination ~86° around Mars, with periapsis at ~300 km and

49   apoapsis at ~10000 km. MARSIS is able to run in either a Sub-Surface mode or an Active

50   Ionosphere Sounding mode. In the latter mode, which we are interested in here, the radar has

51   provided numerous observations of the Martian ionosphere since August 2005 (e.g. Morgan et

52   al., 2008; Němec et al., 2010; Sanchez-Cano et al., 2016). During topside sounding, a 40 m tip-

53   to-tip dipole antenna sweeps through a frequency table (160 steps from 0.1 to 5.4 MHz, with

54   resolution $\Delta f/f \approx 2\%$) during 1.26 s by transmitting 91.4 μs long sinusoidal pulses in a broad

55   angular interval centered on nadir. The radio waves at a given frequency propagate, affected by

56   dispersion (including varying group velocity and ray path bending), through the plasma layers of

57   increasing plasma frequency until the local plasma frequency matches the pulse frequency, at

58   which reflection occurs. Pulse reflection back to the radar nominally occurs at normal angle to

59   the plasma layer. Two types of echoes can be detected at the same time: vertical echoes which

60   reflect from the ionosphere below MEX (assumed to be ideally horizontally stratified) and

61   oblique echoes which reflect from nearby non-horizontal density structures. The receiver

62   measures the time delay for receiving the echo, in 80 bins of duration 91.4 μs starting 253.9 μs

63   and ending 7.56 ms after the start of the pulse. Full frequency sweeps are repeated at 7.54 s

64   cadence. The basic measurement unit is a matrix of received power spectral density versus time

65   delay and frequency, called an ionogram. In this mode, the topside sounder samples plasma

66   layers of increasing density as altitude decreases, from the spacecraft down to the ionospheric

67   peak, according to the relationship $f_p = 8980 \sqrt{N_e}$ between electron density N_e in cm^{-3} and

68   plasma frequency f_p in Hz.

69   This study focusses on localized density structures associated with regions of near radial

70   crustal magnetic fields, detected by MARSIS via oblique echoes, in the dayside Martian

71   ionosphere (Andrews et al., 2014; Diéval et al., 2015; Duru et al., 2006; Gurnett et al., 2005;

72   Nielsen et al., 2007a; Venkateswara Rao et al., 2017). When the spacecraft moves toward or

73   away from such reflecting target, two echoes (one vertical and one oblique) are received, with

74   the time separation between the echoes either decreasing or increasing. When the spacecraft

75   passes directly over the structure, only one echo is detected; the echo may be vertical or oblique

76   depending on the inclination of the plasma layer at each reflection point along the structure. This

77   behavior is characterized by downward facing hyperbola signatures in echograms, which are

78   displays of received intensity at a fixed frequency as function of time and echo range. In

79   echograms, one can usually see that for a given frequency, the apex of the hyperbola appears to

80   stand at or above the surrounding normal ionosphere (rms 19 km higher at a fixed frequency 1.8

81   MHz according to Duru et al., 2006). The apparent altitude of the ionospheric echoes is

82   calculated as the spacecraft altitude minus the echo range assuming speed of light in a vacuum.

83   Gurnett et al. (2005) and Duru et al. (2006) exploited the higher apparent altitude of these

84   structures to interpret them as bulges. Such plasma layers are inclined at a range of angles to the

85   horizontal, up to 90° (Nielsen et al., 2007a). In addition, Venkateswara Rao et al. (2017) reported

86   that the main ionospheric layer and the topside layers at higher altitude (topside layers

87   discovered by Kopf et al., 2008, in the MARSIS data) may both cause oblique echoes in areas of

88   near radial crustal fields, indicating that the density contours of these topside layers can also be

89   tilted.

90   The density structures have regularly been observed over periods of tens of days through

91   subsequent MEX passes above the same magnetized areas, even though the upstream conditions

92   were changing, indicating long term stability (Andrews et al., 2014). They occur above the

93   strong magnetic anomalies of the Southern hemisphere as well as above the weak magnetic

94   anomalies of the Northern hemisphere and their latitude extent matches rather well with the

95   latitude extent of areas of near-radial fields of a given polarity (upward or downward oriented)

96   (Diéval et al., 2015). It is therefore inferred that these structures are not single points, but are

97   spatially extended and confined by the areas of magnetic cusps, reaching horizontal sizes of a

98   few hundreds of km along the spacecraft footprint (Diéval et al., 2015). Oblique echoes are

99   found in regions which have statistically low to moderate rates (20-50%) of open field lines

100 (field lines with one footprint in the crust and the other connected to the IMF) (Diéval et al.,

101 2015). This indicates that their regular occurrence does not depend on the infrequent magnetic

102 reconnection between the crustal fields that rotate with the planet and the variable IMF. In

103 addition, Diéval et al. (2015) reported simultaneous in situ observations of suprathermal electron

104 distributions by the Electron Spectrometer (ELS) (Barabash et al., 2006) onboard MEX which

105 indicated that the plasma regime (ionosphere or shocked solar wind) at the location of MEX

106 (depending on the spacecraft position relative to plasma boundaries) had no influence on the

107 observability of oblique echoes. Solar wind electron precipitation depends on the time-dependent

108 magnetic reconnection between near-radial crustal fields and IMF to reach low altitudes along

109 open field lines (which would otherwise be closed at other times, see e.g. Brain et al., 2007).

110   These recent results do not support the hypothesis proposed by earlier studies (Duru et

111   al., 2006; Gurnett et al., 2005) that solar wind precipitation into magnetic cusps is the primary

112   driver of these density structures. Gurnett et al. (2005) and Duru et al. (2006) had suggested that

113   the solar wind penetrating to low altitude along open field lines would ionize and heat the

114   neutrals, the latter causing an inflation of the neutral atmosphere (which moves additional EUV-

115   ionizable material to higher altitude), such as to generate electron density bulges.

116   Other formation mechanisms have been proposed. If solar wind precipitation is involved,

117   the resulting increase in electron temperature at the altitude of energy deposition causes a

118   reduction of the ion-electron recombination rate, which increases the plasma density (Andrews et

119   al., 2014). Another source of temperature increase may be Joule heating from field-aligned

120   currents and Pedersen currents in regions of magnetic cusps (Fillingim et al., 2010, 2012;

121   Riousset et al., 2013, 2014; Withers et al., 2005). Finally, a 2-D ionospheric model taking plasma

122   transport into account (Matta et al., 2015) has shown that an expanded ionosphere may form in

123   regions of vertical crustal fields via upward diffusion, because it is easier for plasma to move

124   along field lines than across them.

125   The previous studies of oblique echoes were carried out at a fixed frequency, though

126   Nielsen et al. (2007a) reported that during simultaneous observations of vertical and oblique

127   echoes, the maximum frequency of the oblique echo was often smaller than the maximum

128   frequency of the vertical echo. This was interpreted as off-nadir reflections from density

129   structures more tilted to the vertical at low frequencies than at high frequencies. However, there

130   has been no systematic study of the frequency variation of the density structures so far. Since

131   low frequencies correspond to high altitudes and high frequencies to low altitudes, the variations

132   of these structures with altitude remain ambiguous. Also, it has been previously assumed that the

133   oblique echoes are reflected from bulges, because a given electron density level stands at a

134   higher apparent altitude than the surrounding ionosphere. But, the apparent altitude estimation

135   assumes that the pulse propagates at the speed of light in vacuum c, i.e. without correction for

136   dispersion effects in the ionosphere. However, radio waves of frequency f will propagate with a

137   group velocity V_g through an ionized medium of varying refractive index $n = \sqrt{1 - \left(\frac{f_p}{f}\right)^2}$. The

138   group velocity $V_g = c\,n = c\sqrt{1 - \left(\frac{f_p}{f}\right)^2}$ is less than the speed of light and becomes vanishingly

139   small when f approaches f_p, at which signal reflection occurs. For a given time delay, the

140   apparent range of the echo is therefore an upper limit for the real range. Correcting the altitude

141   for dispersion confirms whether or not the density structures really stand higher than the

142   surrounding ionosphere, and by how much.

143   The aim of the current work is to determine the correct shape and magnitude of the

144   altitude changes across the structures as a function of frequency, and thus as a function of

145   altitude, from the high densities near the ionospheric peak down to the lowest densities

146   measurable by the topside sounding technique. This information may provide insight into the

147   formation processes of the density structures.

148   The structure of the paper is as follows: the method is described in Section 2; the results

149   are presented in Section 3 (divided into 3 subsections: A) Close look at individual events, B)

150   Statistics, and C) Influence of crustal magnetic field orientation) and discussed in Section 4.

151   Finally, we summarize in Section 5.

152

153   2) Method

154   Examples of hyperbola signatures from three density structures are shown in Figure 1.

155   The time series runs from 13:00 to 13:15 Universal Time (UT) on 22 July 2006, orbit 3253.

156   During the pass, MEX traveled above moderate strength magnetic anomalies from 46° to -9°

157   latitude at a nearly fixed E. longitude of 350°, inbound toward periapsis (periapsis at 324 km

158   altitude at 13:03:45 UT) and then outbound, on dayside. The altitude varied from 362 km to 709

159   km and the solar zenith angle (SZA) varied from 33° to 48°. Panel (a) shows the crustal magnetic

160   field model of Cain et al. (2003) evaluated at 150 km altitude at MEX footprint, with the

161   magnetic zenith angle (left axis, black curve) and the magnetic field strength (right axis, red

162   curve). The magnetic zenith angle is the angle of the magnetic field vector relative to the zenith:

163   0° is vertical upward, 90° is horizontal. Panels (b), (c), (d) and (e) show MARSIS echograms at

164   four frequencies: 1.52, 1.979, 2.548 and 3.03 MHz, equivalent to electron densities of 2.86×10^4,

165   4.86×10^4, 8.05×10^4 and 1.14×10^5 cm^{-3}, at the reflection point, respectively. The vertical axis

166   is the apparent altitude and the color codes the received intensity.

167   In all echograms, the vertical echo from the assumed ideally horizontally stratified

168   ionosphere is identified as the bright yellow-red trace at near constant apparent altitude (varying

169   from 100 down to 50 km as frequency increases).At frequency 1.52 and 1.979 MHz (panels b, c),

170   three hyperbola signatures are visible, with apexes at 13:03:08, 13:08:39 and 13:12:03 UT. The

171   signatures are marked with black ellipses. At 150 km altitude, the modeled field strength and

172   magnetic zenith angle for these structures are: 109 nT and 166° at 13:03:08 UT, 194 nT and 12°

173   at 13:08:39 UT, and 48 nT and 45° at 13:12:03 UT (panel a). So these density structures are

174   located in regions of near-vertical to oblique crustal fields, consistent with previous reports (e.g.

175   Gurnett et al., 2005). We note that the oblique echoes tend to be more pronounced at low

176   frequencies than at high frequencies. Indeed, there is only one hyperbola signature visible at

177   2.548 and 3.03 MHz (panels d, e). This indicates that the density contours are more inclined for

178   low densities than for high densities, and therefore more able to give oblique echoes, in

179   agreement with Nielsen et al. (2007a).

180   We have conducted a statistical study of a list of oblique echoes previously examined by

181   Andrews et al. (2014) and Diéval et al. (2015). The original list from Andrews et al. (2014)

182   contains 1126 events, detected when MEX was on dayside (SZA < 90°) with an altitude < 1100

183   km, spanning August 2005 to February 2013. The limit at 1100 km comes from the maximum

184   range for which MARSIS can receive ionospheric reflections due to the time delay measurement

185   window. The present study considers 1066 events from this list for which the hyperbola apexes

186   stand at or above the surrounding ionosphere, as determined by Diéval et al. (2015). This ensures

187   that we only look at density structures found directly below the spacecraft. We examine the

188   density structures as a function of frequency (i.e. as a function of altitude); for convenience we

189   need to look at all events in the same frequency bins, so we keep data starting from 1 October

190   2005, after which the MARSIS frequency table became fixed: we keep 901 events from the

191   previous list. It is convenient to work with frequencies here because the altitude of a plasma

192   layer at a given frequency depends on many factors, including SZA, EUV intensity, strength and

193   orientation of local magnetic field, distance of the planet from the Sun, etc..

194   The difference in apparent altitude between the hyperbola apexes and the normal

195   surrounding ionosphere is usually positive and of the order of 19 km (e.g. Duru et al., 2006),

196   which led to the assumption that the density structures are bulges. We want to check this

197   assumption with the altitude measurement corrected for dispersion. The measured time delays

198    $\Delta t(f)$ as a function of frequency can be inverted to obtain the frequency (and density) profile as

199   a function of corrected altitude $z(f_p)$, referred to as the Electron Density Profile (EDP). The

200   Abel transformation gives the solution $z(f_p) = \frac{2}{\pi} \int_{\alpha_0}^{\frac{\pi}{2}} c\Delta t(f_p \sin \alpha) d\alpha$ (Budden, 1961), where

201    $\sin \alpha_0 = \frac{f_p(SC)}{f_p(max)}$. The integration in frequency goes from the local plasma frequency at the

202   spacecraft $f_p(SC)$ to the maximum plasma frequency of the ionosphere $f_p(max)$.

203   There are several challenges associated to the detection of the ionospheric reflection at

204   low frequencies, and thus to their inversion. The local plasma frequency is obtained from the

205   MARSIS plasma oscillations excited in the antenna (e.g. Gurnett et al., 2005). These harmonics,

206   recognizable as vertical bright stripes in MARSIS ionograms, make the estimation of reflection

207   time delays more difficult at low frequencies. Electron cyclotron harmonics are also detected as

208   horizontal bright stripes in MARSIS ionograms, when MARSIS is exposed to local magnetic

209   fields of strength larger than a few tens of nT (Gurnett et al., 2005); these interferences again

210   hinder the visibility of the ionospheric echo at low frequencies (the problem is even more acute

211   above the magnetic anomalies, where we conduct the present work). Finally, the transmitted

212   power falls off sharply at low frequencies, which makes the reflected signal often too low to be

213   detectable at frequencies < ~1 MHz (e.g. Morgan et al., 2013). These circumstances of low

214   signal to noise ratio lead to a data gap between the local plasma frequency measured at MEX

215   location and the lowest frequency measurable with the ionospheric reflection. The error on the

216   determination of the corrected altitude becomes large if the frequency range of the gap is

217   significant compared to the frequency range of the reflection (e.g. Morgan et al., 2013).

218   The density profiles presented here were obtained with the inversion method by Němec et

219   al. (2016a), itself derived from the standard inversion method by Morgan et al. (2013). The

220   inversion process in these methods assumes that the pulse propagates along the nadir direction

221   (vertical echo), the ionosphere has plane parallel stratification, there are no magnetic effects, and

222   the density profile monotonically increases as altitude decreases. We note that the existence of

223   non-monotonic density profiles presenting transient topside layers above the main density peak,

224   for which the assumption of monotonic profiles is not valid (e.g. Kopf et al., 2008). Also, the

225   plane parallel approximation breaks down near the terminator, where the plasma density is

226   weaker and more variable than on dayside (e.g. Fox and Yeager, 2006; Gurnett et al., 2005). In

227   addition, near the terminator, MARSIS sometimes detects ionospheric echoes and ground echoes

228   overlapping for a range of frequencies, which can be explained by the strong horizontal density

229   gradients present at the terminator (Duru et al., 2010). In this case, a single ionospheric reflection

230   is observed, which is not vertical, but off-nadir. Finally, the lower densities near the terminator

231   or at high spacecraft altitude increase the frequency range of the data gap compared to the

232   measured frequency range of the ionospheric reflection, making the inversion process more

233   error-prone.

234   For these reasons, Morgan et al. (2013) considered EDPs as unreliable for SZA > 85° or

235   spacecraft altitude > 800 km. In practice, this means that they rejected profiles for which the

236   frequency range of the gap is larger than the frequency range of the ionospheric echo and/or

237   larger than 1 MHz. In addition, Morgan et al. (2013) have excluded profiles with ionospheric

238   peak frequencies between 2.25 and 2.3 MHz, for which there is a sensitivity gap. Since the

239   terminator region causes many difficulties, we restrict our study to SZA < 85°: this leaves 890

240   events to study. The major difference between the two mentioned inversion methods is the

241   functional form used for $f_p(z)$ in the low frequency data gap. The reader is directed to Němec et

242   al. (2016a) for details.

243   Finally one may question whether the assumptions of vertical reflection and plane

244   parallel stratification are reasonable in regions of density structures (with inclined density

245 layers). We discuss the problem and make a check of these assumptions in appendix A. The

246 conclusion of this check is that for the events investigated in this work, the assumption of plane

247 parallel stratification is definitively good, and the assumption of vertical propagation is good

248 enough to use as an approximation. Therefore we trust these EDPs are appropriate for this study.

249   We want to look at time series of EDPs for each density structure, by selecting all

250 available EDPs (from the processing by Morgan et al., 2013) during the period for which the

251 spacecraft passes overhead the structure. For this purpose, we need the echograms, which we

252 integrate over a range of frequencies typical for oblique echoes (we chose between 1.8 and 2

253 MHz), rather than just taking one frequency level, because it improves the noise/ratio of the

254 echogram (less background noise and more pronounced ionospheric traces, resulting from

255 combining different frequencies) and shows ionospheric features which could possibly be missed

256 if using only one frequency level. This period of overhead pass is estimated from the MARSIS

257 echograms by considering the time at which the hyperbola signature starts merging and then

258 stops merging with the main surrounding ionosphere echo. This exercise is a rough estimate (but

259 good enough for our purpose) because of the following difficulties. 1) The merging time for each

260 hyperbola leg can take the duration of several ionograms (several times 7.54 s), and is thus not

261 instantaneous or easy to determine. 2) Several structures can be superposed on top of each other

262 due to the frequent occurrence of oblique echoes in neighboring regions of alternating radial field

263 polarities; this makes it difficult to separate individual structures. 3) The structure can present

264 only one clear leg or present one or two short/unclear legs, which make it hard to determine

265 where are the edges of the structure. 4) In practice, the period of overhead pass is itself limited

266 by the coverage of available EDPs during this period. From the previous list, there are 165 events

267 for which there are at least 3 available EDPs to make a time series. Figure 2 shows the state of

268   the EDP coverage for these 165 events. Panel (a) shows the distribution of the duration of events

269   for all the events as estimated from the procedure above (panel a), which is broad with a tail at

270   high values, median of 90 seconds, and minimum and maximum values of 30 and 242 seconds

271   respectively. Such durations of one to several minutes are consistent with the previous report by

272   Diéval et al. (2015). Panel (b) shows the restrictions from the processing by Morgan et al. (2013)

273   is such that there are not always as many EDPs available as one would wish for a complete

274   coverage of each event. The distribution of the number of available EDPs divided by the number

275   of ionograms during the duration of each event (i.e. ratio of numbers), for all the events, is broad

276   with a median of 0.58 and minimum and maximum values of 0.12 and 1 respectively.

277   It is preferable not only to have a good proportion of EDPs available (to reduce the data

278   gaps) but also to have the first and last available EDPs covering as close to the beginning and

279   end (edges) of the overhead pass as possible. Panel (c) shows the distribution of the duration of

280   the EDP coverage divided by the event duration for each event (i.e. ratio of durations), for all the

281   events, peaking at high values, with a median of 0.85 and minimum and maximum values of 0.14

282   and 1 respectively; so a majority of events has available EDPs rather close to the edges of the

283   structure, which is a good sign. Panel (d) shows a scatter plot of the ratio of durations plotted

284   versus the ratio of numbers, colored by the number of available EDPs for the duration of each

285   event, for all the events. Naturally, the number of available EDPs increases as both ratios

286   increase. We decide to keep 48 events for which the number of available EDPs divided by the

287   number of ionograms is ≥ 0.7 and for which the duration of the EDP coverage divided by the

288   event duration is ≥ 0.7. For these 48 events we are confident we have a reasonable EDP

289   coverage, and therefore a reasonable determination of the shape of the time series of EDPs. The

290 minimum and maximum values of the number of available EDPs per event become 4 and 20

291 respectively.

292   We will compare the altitude variations for the EDPs of the time series for each event, at

293 a fixed sounding frequency, for all frequencies for which ionospheric traces were detected (the

294 local frequency is excluded from analysis). To make it easier to identify the shapes of density

295 structures, we visually inspect these time series at a few selected frequencies typical for the

296 detection of oblique echoes, to select one EDP which defines best the simplest shape of the time

297 series, in comparison with the first and last EDPs (beginning and end edges) of the time series

298 (i.e. using three EDPs to find the simplest shape). This selected EDP is thus a reference profile to

299 which we compare the other EDPs in the time series, and is referred to as "point of interest" PI

300 EDP. By choosing the PI EDP in this manner, we do not require the PI EDP to sit at the center of

301 the time series nor at the apex of the hyperbola signature (so there can be unequal numbers of

302 EDPs on either sides of the PI EDP). The determination of the PI EDP is somehow subjective,

303 especially if the shape of the time series is complicated, with complex variations; in addition the

304 shape can change with increasing frequency, although gradually. Anyway this exercise is made

305 for helping identify the altitude variations relative to a reference EDP.

306   At a fixed frequency, the 4 simplest possible shapes are as follows. 1) If the altitude of

307 the PI EDP is higher than the altitude of both beginning and end EDPs, then we call the shape

308 "bulge". In this case, there is first an increase and then a decrease of the altitude level, the PI

309 EDP having the highest altitude in the time series. 2) If the altitude of the PI EDP is lower than

310 the altitude of both beginning and end EDPs, then we call the shape "dip". In this case there is

311 first a decrease then an increase in altitude, the PI EDP having the lowest altitude in the time

312 series. 3) If the altitude of the PI EDP is higher than the altitude of the beginning EDP and lower

313   than the altitude of the end EDP, then we call the shape "uphill slope". 4) If the altitude of the PI

314   EDP is lower than the altitude of the beginning EDP and higher than the altitude of the end EDP,

315   then we call the shape "downhill slope". The PI EDP for an uphill slope or downhill slope is

316   determined visually from the EDP bringing a change of slope along the time series, i.e. this EDP

317   can be used to test if the slope is convex or concave. The four possible simplest shapes

318   mentioned: bulge, dip, uphill slope and downhill slope, have been found in the 48 events we

319   have examined, as we will see below.

320   In the following figures, for a given event, we either use the altitude differences between

321   the PI EDP and all other EDPs in the time series for a detailed study, or we use the altitude

322   differences between the PI EDP and the beginning or end EDPs (edges) for a more concise

323   study. Several times we will work at a fixed frequency 1.936 MHz, for illustration of a typical

324   frequency at which oblique echoes are detected. We note that the uncertainty on the range of the

325   ionospheric echo corresponds to one pixel and is given by $c \times \Delta t/2 = 13.7$ km $= \pm 6.9$ km. For

326   this work, it means that, for an event at a fixed frequency, if the absolute value of the altitude

327   difference between the PI EDP and another EDP of the time series is larger (smaller) than 13.7

328   km, then this altitude difference is resolved (unresolved) by the measurement.

329

330   3) Results

331   A) Close look at individual events

332   In this subsection, we investigate the detailed variations of a few events as a function of

333   frequency and time. Figure 3 shows time series in 4 columns corresponding each to one example

334   of event with a rather clear shapein EDP time series at different frequency levels (see top row):

335   (a) bulge, (b) downhill, (c) dip and (d) uphill. The date and time of PI EDP for each event are

336   indicated in the figure. In all panels, the vertical dashed lines mark particular measurement times:

337   PI EDP (magenta), beginning and end EDPs (black), beginning and end times determined from

338   the echogram (green). The top row shows time series of EDPs color coded for 6 selected

339   frequencies between 1.433 and 2.505 MHz. Our working frequency of 1.936 MHz lies between

340   the green and magenta curves.

341   We see that bulges are indeed detected, consistent with expectations from using the

342   uncorrected apparent altitude (e.g. Duru et al., 2006). Interestingly, other shapes are also

343   detected: dips (as proposed by Nielsen et al., 2007a), uphill and downhill slopes; in principle

344   their inclined density contour levels are able to give oblique echoes. We see sometimes complex

345   altitude variations which tend to complicate the shape of events, but the simplest shapes were

346   rather easy to determine for these 4 cases. For example, the dip event in column (c) appears more

347   clearly as a dip if one considers the gradual decrease and then gradual increase of altitude on

348   either side of the PI EDP, with the gradual decrease being shortly interrupted by an amplitude

349   quirk. As we see already here, and will see again later, that the altitude variations tend to be

350   larger at low frequency (high altitude) than at high frequency (low altitude), and the shape can

351   remain the same at all frequencies or change with frequency.

352   The second row of Figure 3 shows the time series of altitude differences between the PI

353   EDP and the other EDPs of the time series for these 4 events, at a fixed frequency 1.936 MHz.

354   Positive values mean that the PI EDP stands at higher altitude than these EDPs, negative values

355   mean that the PI EDP stands at lower altitude than these EDPs, zero values correspond to the PI

356   EDP or any EDP with identical altitude. For clarity, the magenta vertical dashed line indicates

357   the position of the PI EDP. At frequency 1.936 MHz, there are 33 events out of 48 classified as

358   bulges, 6 as dips, 4 as downhill slopes, 3 as uphill slopes, and 2 undetermined (data gap). As we

359   will see later, at this frequency the bulges dominate the number of events, compared to other

360   shapes. Interestingly, this result, based on altitude profiles corrected for dispersion, confirms the

361   insights of Gurnett et al. (2005) and Duru et al. (2006) based on the apparent altitudes

362   uncorrected for dispersion.

363   In the bottom row of Figure 3, we inspect the hyperbola signatures in the echograms

364   integrated for 1.8-2 MHz for these 4 events. These panels have an extended time range to give a

365   better view of the oblique echoes caused by the density structures. While the hyperbola signature

366   in column (a) presents two clear legs (here there is a bulge), the hyperbola signature in the other

367   columns have only one clear leg, with the leg at the beginning of the signature for column (c)

368   (here there is a dip) or the leg at the end of the signature for columns (b) and (d) (here there are

369   downhill and uphill slopes respectively). We also see that the point of highest apparent altitude

370   on the hyperbola signature does not necessarily correspond to the highest (or even lowest)

371   altitude point (for bulges and dips) in the time series of corrected altitudes from the top row.

372   Examination of the other events in the list suggests two points. 1) The variations of the apparent

373   altitude of the hyperbola signature on the echogram bear no predictable relation to the variations

374   of the corrected altitudes in the same frequency range. 2) The presence of two clear hyperbola

375   legs or only one clear leg at the beginning or end of the structure cannot be reliably related to the

376   simplest shape of structures in the same frequency range. One could have expected, from

377   considerations of spacecraft motion moving toward and then away from a structure, that the

378   slopes on either side of a bulge or dip should cause 2 clear legs at the beginning and end of the

379   structure, while an uphill slope would cause just one clear leg at the beginning of the structure

380   and a downhill slope would cause just one clear leg at the end of the structure. It is likely that the

381   key to understand these two issues arises from both the signal dispersion (including varying

382   group velocity and ray path bending as the plasma frequency of the medium changes during their

383   propagation) and the likely complicated geometry of the ray paths related to the presence of

384   horizontal density gradients (possible multiple reflections for a given ray). Ray tracing through

385   models of ionospheric layers obtained from the MARSIS measurements, taking signal dispersion

386   into account, would be illuminating to solve these two issues, although it is beyond the scope of

387   the present work.

388   In Figure 4 we check the EDPs for their full frequency range for the same 4 events.

389   Figure 4 displays the series of EDPs for each event into four panels: bulge (a), downhill slope

390   (b), dip (c) and uphill slope (d). For each event, the red curve is the PI EDP, the black curves are

391   the other EDPs for the time series, the colored dots mark the same data points (color coded with

392   frequency) as in Figure 3. For each event, the EDPs are plotted versus $\log_{10}$(density) in cm^{-3} and

393   the densities of the successive EDPs are multiplied by 10^{0}, 10^{1}, 10^{2}, etc., for clarity. Because this

394   way of displaying EDPs is equivalent to a time series of EDPs, one can see that for each event,

395   the shapes of the color coded altitude variations at the various frequencies follow the same

396   shapes as in Figure 3. We remark for these 4 events (noticed also for the other events in the list)

397   that the altitude range of these EDPs actually shifts down or up in altitude to follow the shape in

398   the time series of EDPs from Figure 3; the ionospheric peak altitude tends to follow this trend

399   too. For example, for the bulge event the altitude range of each EDP shifts upward until the PI

400   EDP is reached, then the altitude range of the following EDPs shifts down, like the entire topside

401   ionosphere moves up then down in altitude. Similarly, the entire topside ionosphere appears to

402   continuously move up for the uphill event, continuously move down for the downhill event and

403   first move down then move up for the dip event. We note that the absolute value of the

404 difference in SZA between the first and last EDPs of the time series for each event is typically

405 small, with a median of 1.6°, thus these altitude changes are independent of the SZA.

406   When examining the EDPs for the overall of events of the list, there are sometimes hints

407 of vertical gradients in the form of slight ledges, for example at 220 km altitude for the 5th EDP

408 from the left in panel (d). These vertical gradients may be density bite-outs, density bumps and

409 topside layers (e.g. Kopf et al., 2008, Withers et al., 2005) which would have been attenuated in

410 the EDPs because of two reasons. 1) When there is a non-monotonic variation in the electron

411 density (i.e. a valley: decrease in density as altitude decreases above the main peak), MARSIS

412 cannot observe this valley directly because low frequency signals get reflected at layers of larger

413 plasma frequency present at higher altitudes above the valley, although indirect observations are

414 possible (e.g. Wang et al., 2009), 2) the processing of the EDPs by Morgan et al. (2013) assumes

415 monotonic profiles.

416   We examine the trends of ionospheric peak altitude and peak frequency for the same 4

417 events in Figure 5, which is organized as columns: (a) bulge, (b) downhill slope, (c) dip, (d)

418 uphill slope. The first row has almost the same format as the first row of Figure 3. The second

419 and the third row show time series of peak frequency and peak altitude, respectively. For these

420 events, the variation of the peak frequency presents no clear relationship compared to the

421 variation of the altitude levels at a few lower frequencies: although the peak frequency tends to

422 increase during the bulge event, the peak frequency just increases during the downhill slope

423 event, also just increases during the dip event and stays constant during the uphill event. From

424 looking at the rest of the events in the list, there is no systematic increase (or decrease) in peak

425 density in the regions giving oblique echoes. We note that individual cases of high peak densities

426 in areas of strong near vertical crustal fields were reported by e.g. Nielsen et al. (2007b). On the

427   other end, the evolution of the peak altitude for the 4 events tends to follow the variations of

428   altitude levels at lower frequencies, such as to track the shape of the time series of EDPs. This

429   trend was observed as well for the rest of the events in the list.

430   Finally, the evolution of the simplest shape of events with frequency is also examined for

431   the full frequency range of a few selected events. Figure 6 shows the shape classification of 6

432   events as function of frequency, displayed as colored dots: bulge (red), concave slope (green),

433   convex slope (blue) and dip (black). Here we use the altitude differences between the PI EDP

434   and the first or last EDP of the time series, at a fixed frequency, for every frequency of each

435   event. It is useful to consider the convex or concave nature of a slope here, because a convex

436   slope swells downward (looks like a dip) and a concave slope swells upward (looks like a bulge).

437   For a given slope event, at a fixed frequency, the event is determined as convex (concave) if the

438   second derivative of the altitude from the time series of three EDPs is positive (negative). The

439   date and time of the PI EDPs are indicated in each panel. In panels (e) and (f), the event remains

440   with the same shape at all frequencies: bulge and dip, respectively. In panel (a), the event

441   evolves from concave, to bulge then to concave, as frequency increases. In panel (c), the event

442   evolves from convex, to concave, then to bulge. In panel (b), the event evolves from concave, to

443   convex, to dip, to convex, and then to concave. In panel (d), the event evolves from concave, to

444   bulge, to concave, to convex, and then to concave.

445   It is observed that the shape change is gradual such that there are always concave and

446   convex slopes in the correct order to separate bulges and dips; this is natural since a concave

447   slope looks like a bulge and a convex slope looks like a dip. This is confirmed by examining the

448   other events in the list. We see that in the case of events changing shape over frequency: if the

449   shape is not a bulge in a given segment of the frequency range, there is no marked preference for

450   observing dips rather than convex slopes or concave slopes. This holds for the entire frequency

451   range. Note that the shape of an individual event at a fixed frequency may be uncertain if the

452   altitude differences are unresolved, i.e., in absolute value are lower, than the 13.7 km range

453   resolution (this is the case for many events as we will see later). Despite this, there is a

454   systematic gradual transition over frequency. This result validates the determination of shape

455   over frequency for individual events, whatever the magnitude of the altitude differences.

456

457   B) Statistics

458   Now we consider all the events for statistics purposes. We start with inspecting the

459   magnitude of the altitude differences for all the events as a function of frequency for the entire

460   frequency range. Figure 7 shows in panels (a, b) the altitude differences between the PI EDP and

461   the edge EDP of each event, versus frequency, for all the events, and similarly, in panels (c, d),

462   the altitude differences between the PI EDP and the edge EDP relative to the altitude of the PI

463   EDP of each event. The edge EDP is either the first or last EDP of the time series of a given

464   event. Altitude differences which change sign over frequency are plotted in panel (b, d), while

465   altitude differences keeping the same sign over frequency are plotted in panel (a, c). Median

466   values of the altitude differences over frequency are indicated by red dots. The median values of

467   the altitude differences being all positive or all negative over frequency are treated separately.

468   Horizontal black dashed lines delimitate regions where the absolute values of altitude differences

469   are > or < 13.7 km (13.7 km is the range resolution). Colored patches in panels (a,b) help

470   distinguishing these regions of resolved or unresolved altitude differences (cyan or white).

471   In panels (a, c), the altitude differences tend to be larger in absolute value at low

472   frequency than at high frequency, both for all-negative and all-positive differences. These trends

473   are also reproduced by the medians values. The largest values of altitude differences (several

474   tens of kilometers or several tens of % relative to the PI EDP) are found at low frequencies, and

475   the lowest values (several kilometers or several % relative to the PI EDP) at high frequencies.

476   Thus, it is more likely for the altitude differences to be unresolved (< 13.7 km) at high

477   frequencies (low altitudes) than at low frequencies (high altitudes). The absolute value of the

478   median of altitude differences becomes larger than 13.7 km at a fixed frequency of 1.848 MHz

479   (1.805 MHz) for the all-negative (all-positive) altitude differences. Finally, a majority of altitude

480   differences lie completely within the unresolved region (cyan patch). Similarly, for the altitude

481   differences changing sign over frequency (panels b, d), the altitude differences tend to be larger

482   in absolute value at low frequency than at high frequency. These trends are also reproduced by

483   the medians values. The contribution of both negative and positive values at each frequency

484   contributes to decrease the absolute value of the median, to be below 13.7 km. The results are

485   consistent with the finding by Nielsen et al. (2007a) of density contours being more tilted at low

486   frequencies than at high frequencies.

487   In Figure 8, we check the distributions of altitude differences between the PI EDP and the

488   edge EDP, for all the events, separated between the 4 simplest shapes, at 4 different frequencies

489   corresponding to 4 panels: (a) 1.411, (b) 1.848, (c) 2.155 and (d) 2.854 MHz. In each panel, the

490   distributions are color coded per shape and plotted as stacked bars on top of each other in every

491   bin: bulge (red), black (dip), downhill slope (green) and uphill slope (blue). Regions of

492   abs(altitude differences) < or > 13.7 km are delimited by thin vertical black dashed lines and

493   colored patches (unresolved: cyan, resolved: white). For bulges, both sides of the structure has

494 positive values of altitude differences; similarly for dips both sides have negative values of

495 altitude differences; for uphill slopes the value of altitude difference is positive for the first EDP

496 and negative for the last EDP; for downhill slopes the value of altitude difference is negative for

497 the first EDP and positive for the last EDP. At the 4 frequencies shown, the number of bulges

498 dominates the number of other shapes (we will see this also later). As frequency increases, the

499 spread of altitude difference values tends to decrease for each shape, with less extreme values

500 present, such that the distributions become more confined within the region of abs(altitude

501 differences) < 13.7 km (cyan). At a fixed frequency, the absolute value of the altitude differences

502 tends to be larger for bulges than for other shapes, and tends to be larger at low frequency than at

503 high frequency for bulges but less evident for other shapes (see also the median values for the 4

504 distributions of simplest shapes indicated as color coded text in each panel). There may be an

505 effect of the number of events regarding the trends of bulges versus other shapes, since there are

506 far more bulges than other shapes, as we will see later. For illustration, the median value of 12.4

507 km for the altitude differences in bulges at a fixed frequency 1.848 MHz is of the same order as

508 the rms apparent altitude difference between the hyperbola apex and the main ionosphere of 19

509 km at a fixed frequency 1.8 MHz determined by Duru et al. (2006).

510 We also examine, in Figure 9, the distribution of the four simplest shapes of all events in

511 the entire frequency range, displayed as color coded symbols: bulges (red dots), dips (black

512 diamonds), downhill slopes (green '+'), uphill slopes (blue 'x'). The number of events drops

513 sharply at frequencies below 1 MHz because of the various issues of signal to noise ratio

514 mentioned earlier, and drops sharply at frequencies above 3 MHz (1.1×10^5 cm^{-3}) because the

515 ionospheric echo is constrained by the peak density (which varies between 0.5 and 1.5×10^5 cm^{-3}

516 on dayside, see e.g. Morgan et al., 2008). The distribution of bulges dominates the total number

517   of events and peaks at 2.111 MHz with 36 events; at the same frequency there are 5 downhill

518   slope events, 1 uphill slope event and 5 dips. The distribution of uphill slope events peaks with 5

519   events at 7 different frequencies those highest is 1.63 MHz, for downhill slope events it peaks

520   with 7 events at 3 frequencies those highest is 1.455 MHz and for dips it peaks with 8 events at 7

521   different frequencies those highest is 1.52 MHz. Thus, the number of bulges peaks at a much

522   higher frequency than the numbers of other shapes does. For frequencies below 0.951 MHz all

523   shapes have comparably small numbers of events. This is likely an effect of bad statistics, since

524   there are challenges for measuring the ionospheric trace at frequencies < 1 MHz. For higher

525   frequencies the number of bulges is much larger than the other numbers. It is worthwhile to note

526   that for the 48 events, there are 20 events detected during MEX passes going from North to

527   South, and 28 events detected during passes going from South to North; still the proportions of

528   uphill and downhill slope events remain similar in both instances, as expected.

529   Finally, we can compare the behaviors of the ionospheric peak altitudes and peak

530   frequencies to the behavior of the altitude level at 1.936 MHz, for all the events, to check the

531   case studies trends from Figure 5. Then, Figure 10 shows scatter plots of the altitude level at

532   1.936 MHz versus the peak frequency (panel a) and versus the peak altitude (panel b), both using

533   all the available EDPs in the time series of all the events. As suggested from the inspection of

534   individual events, we see that when the selected altitude level increases, the peak frequency has a

535   weak trend of increase (broad scatter), while the peak altitude has a clear trend of increase

536   (narrow scatter). We confirm that these trends remain visible (especially for the peak altitude)

537   when separating the events into the 4 types of simplest shapes at 1.936 MHz (not shown). For the

538   case of bulges (the majority of events), the peak altitude has a marked tendency of a local

539   increase and the peak frequency has a less evident tendency of a local increase, in areas of

540   oblique echoes.

541

542   C) Influence of crustal magnetic field orientation

543   Previous studies have shown the close association between oblique echoes and near-

544   vertical crustal magnetic fields (e.g. Gurnett et al., 2005). Here we inspect the relationships of the

545   altitude differences in areas of oblique echoes and corresponding magnetic anomalies, first for a

546   few individual events, then for all the events. We use the Cain et al. (2003) crustal magnetic field

547   model evaluated at 150 km altitude at MEX footprint.

548   Figure 11 shows maps of two regions of magnetic anomalies of moderate strength near

549   the equator, in the Southern hemisphere (panel a) and Northern hemisphere (panel b). Selected

550   contours of the angle of the crustal magnetic field to the vertical are displayed using the left side

551   colormap. The horizontal orientation is 0° and the vertical orientation is 90°. Field strengths < 30

552   nT are ignored. The footprints of MEX location at the times of available EDPs for individual

553   events detected in these regions are superposed onto the maps. The location of the PI EDP is

554   marked by a black 'x' for each event and its date and time written in the panels. The events are

555   each colored with the altitude differences between the PI EDP and the other EDPs of the time

556   series relative to the altitude of the PI EDP (in %), all taken at a fixed frequency 1.936 MHz.

557   Negative values mean that the PI EDP stands at altitudes below these EDPs, zero values mean

558   that the PI EDP stands at the same altitude as these EDPs (the PI EDP itself or other EDPs of

559   equal altitude), and positive values mean that the PI EDP stands at altitudes above these EDPs.

560 Negative values are in blue, zero values in white and positive values in red, using the colormap

561 on the right side.

562   In both maps, there are events detected geographically close to each other, at different

563 dates and times, with similar shapes or different shapes, from their altitude differences. Thus the

564 shape may vary in geographical location and time. The range of crustal field orientations,

565 through the latitudinal extension of the events (MEX orbits are nearly fixed in longitude near the

566 equator), covers well the areas of near radial field near the center of the events, and the areas of

567 near horizontal field near their edges. The time of the PI EDP is determined from the timeseries

568 of EDPs, and is not necessarily associated to near vertical fields.

569   Finally, we check whether the magnitude and the sign of the altitude variations at a fixed

570 frequency 1.936 MHz are affected by the crustal field orientation, for all the available EDPs of

571 the time series of all the events, in Figure 12. The data points of the altitude differences between

572 the PI EDP and itself (which are zero values) are removed from this figure, so the zero values

573 which remain are only due to other EDPs with altitudes identical to the PI EDP. Panel (a)

574 displays the distribution of the angle of the crustal field to the vertical, which covers the full

575 range of possible angles (minimum and maximum are 2.5 and 89.5°), with 25th, 50th and 75th

576 percentiles of 26.6, 42.0 and 61.8°, respectively. The distribution peaks at angles closer to the

577 vertical than to the horizontal (it peaks at angles < 45°). This is expected because the density

578 structures giving oblique echoes are usually found in areas of vertical to oblique crustal field

579 orientation, with a latitude extension covering the latitude extension of the magnetic cusps, the

580 magnetic field strength being not important (e.g. Duru et al., 2006, Diéval et al., 2015). The time

581 series of EDPs cover whenever possible up to the edges of the density structures as determined

582   from the echograms, thus angles closer to the horizontal are also sampled, particularly near the

583   edges.

584   Panel (b) shows the distribution of the altitude differences between the PI EDP and the

585   other EDPs of the time series, which presents negative and positive values (minimum and

586   maximum are -24.7 and 44.1 km), peaks at positive values (there is a majority of bulges which

587   contribute positive altitude differences), with 25th, 50th and 75th percentiles of 1.1, 5.8 and 12.3

588   km, respectively. There are 390 data points, whose 309 are positive differences and 76 are

589   negative ones. In absolute value, typically, the smallest altitude differences are found close to the

590   PI EDP, and the largest values close to the edges of the structure. Panel (c) shows the distribution

591   of altitude differences between the PI EDP and the other EDPs of the time series, relative to the

592   altitude of the PI EDP (in %), which shows similar behavior to the former distribution. It

593   presents negative and positive values (-13.5 and 21.2 %, respectively), peaks at positive values,

594   with 25th, 50th and 75th percentiles of 0.6, 2.9 and 6.4 %, respectively.

595   Panel (d) displays a superposed epoch analysis of the angle of the crustal field to the

596   vertical, using the time difference in seconds between the available EDP in the time series and

597   the center time of the density structure (positive values are after and negative values are before

598   the center time, respectively). For each event, the center time is the time at the center of the

599   interval bounded by the edges of the structure as determined from the echogram. A red line

600   indicates the median values of angles as a function of superposed epoch time. The distribution

601   varies like a broad "v" shape, as well as the median values. We have checked that individual

602   time series often vary such as to be centered near a "v" shape. The crustal field orientation

603   changes from more vertical to more horizontal, as one progress from the center of the structures

604   toward their beginning and end edges. This trend is expected, since the latitudinal extension of

605 the structures giving oblique echoes tends to cover the latitudinal extension of the corresponding

606 magnetic cusps (e.g. Diéval et al., 2015).

607 Panel (e) displays a superposed epoch analysis of the relative altitude differences, using

608 the time difference in seconds between the available EDP in the time series and the PI EDP

609 (positive values are after and negative values are before the PI EDP, respectively). A red line

610 indicates the median of the relative altitude differences as a function of superposed epoch time.

611 When considering the majority of points being positive, the distribution varies like a broad "v"

612 shape. We have checked that individual profiles plotted in this way do not necessarily exhibit a

613 clear "v" shape (even when including only bulges), because of the ample fluctuations existing in

614 the time series. The median values also vary as a "v" shape. Since the majority of density

615 structures are bulges, this means that the altitude level at a fixed frequency tends to stand further

616 down (relative to the PI EDP) as one progresses toward both beginning and end edges of the

617 structures.

618 Panel (f) shows a scatter plot of the angle of the crustal field angle to the vertical versus

619 the relative altitude differences. There is no obvious trend here, with an extended range of

620 altitude differences (both for positive and negative ones) whatever the crustal field orientation.

621 Considering the events of the 4 simplest shapes separately does not affect this result (not shown).

622 There is however a slight trend to find the largest positive values toward large angles, i.e. to find

623 the edges of the density structures (mostly bulges) near the edges of magnetic cusps (near

624 horizontal field orientation).

625

626 4) Discussion

627   We have examined the behavior of the density structures from the lowest measurable

628   densities down to the densities approaching the ionospheric peak. The absolute value of the

629   median of altitude differences becomes larger than 13.7 km at a fixed frequency of 1.848 MHz

630   (1.805 MHz) for the all-negative (all-positive) altitude differences between the PI EDP and the

631   edge EDPs; we take the typical transition frequency as the average between these 2 values: 1.826

632   MHz, corresponding to 4.13×10^4 cm^{-3}. This threshold is marked with a vertical red dashed line

633   in Figure 7a.

634   It is important to note that the ionosphere has several regimes depending on altitude. At

635   low altitude near the ionospheric peak (near 125 km altitude at SZA=0°) the plasma is in

636   photochemical equilibrium (electron production rate balances recombination); for ions the

637   transport time is much longer than the chemical loss time. At high altitude the chemical loss time

638   becomes much longer than the transport time because of the reduced densities, the ions are then

639   transported over significant distances before they are lost to chemical reactions: the ionosphere is

640   in the transport regime (above 200 km altitude). We can check the altitude range for the behavior

641   of the density structures and compare it to these regimes. For this purpose, we use the empirical

642   model of the Martian dayside ionosphere by Němec et al. (2011a; 2016b), based on MARSIS

643   AIS EDPs, which incorporates dependencies on the solar radio flux F10.7, the Sun-Mars distance

644   R and the strength of the crustal magnetic field B at 400 km altitude (see

645   http://aurora.troja.mff.cuni.cz/nemec/n11/). We take average conditions since the list of events

646   covers different periods over several Martian years and we use conditions of moderate magnetic

647   anomalies: F10.7=90 sfu, R=1.5 AU and B=30 nT.

648   The altitude of the level 4.13×10^4 cm^{-3} (1.826 MHz) varies from 198 km at SZA=0° to

649   188 km at SZA=85°. Therefore there is a transition altitude of ~ 190 - 200 km on dayside; below

650   (above) this altitude, the altitude differences tend in absolute value to be lower (higher) than 13.7

651   km. Above this altitude range, transport processes are dominant, while below this altitude range,

652   chemical reactions are dominant. In Figure 1, we have illustrated the effect of increasing

653   frequency on the visibility of the hyperbola signatures. For example, at 1.52 MHz (panel b) the

654   signatures are all well pronounced, while at 3.03 MHz (panel e) they become smaller. The

655   altitude of the level for 1.52 MHz (2.86×10^4 cm^{-3}) varies from 217 km at SZA=0° to 207 km at

656   SZA=85°; this altitude range of 207 - 217 km is found within the transport dominated region.

657   The altitude of the level for 3.03 MHz (1.14×10^5 cm^{-3}) reaches 153 km at SZA=0°; this altitude

658   level is found at altitudes where photochemistry prevails. Bulges are the most commonly

659   observed structure in the topside ionosphere, present within the transport region with large

660   altitude differences and present within the photochemical region with small altitude differences.

661   These large and often positive altitude differences PI EDP – edge EDP (> 13.7 km) at

662   altitude above ~200 km can be related to upward diffusion along vertical crustal magnetic field

663   lines, in the altitude range of transport regime. This idea was proposed by Matta et al. (2015),

664   who successfully modeled the formation of density bulges in areas of near radial crustal fields,

665   using a 2-D ionospheric model incorporating field-aligned transport. Matta et al. (2015) found

666   that the altitude difference between the density structure and the surrounding normal ionosphere

667   increases when the altitude increases, starting from ~170 km altitude, i.e. at altitudes where

668   transport becomes important. On the other hand, Matta et al., (2015) did not predict the

669   formation of bulges at altitudes below ~170 km, where they fond the ionosphere to have a

670   photochemical behavior, without any vertical transport effects. In contrast, our observations

671   show the presence of density structures at altitudes below ~200 km, with smaller altitude

672   differences (< 13.7 km) becoming increasingly small as altitude decreases. In addition, the entire

673   topside ionosphere seems to move up and down, including the ionospheric peak, in the areas

674   giving oblique echoes. In these areas, the peak densities did not change predictably. Therefore

675   we need an additional mechanism which may explain these observations in the altitude range of

676   photochemical equilibrium. Such mechanism may be as follows.

677   Previous observations of the Martian dayside ionosphere during periods of global dust

678   storms indicate that the peak altitude and the top of the ionosphere both rise in altitude, while the

679   peak density does not change much (e.g. Hantsch and Bauer, 1990; Wang and Nielsen, 2003;

680   Withers et al., 2015). The top of the ionosphere as defined by Withers et al. (2015) is "the

681   altitude above the peak at which electron densities first fall below 1500 cm^{-3} when moving

682   upward in altitude". These behaviors are interestingly similar to our observations in areas of

683   oblique echoes. The mechanism for the dust storm effects has been described by e.g. Wang and

684   Nielsen (2003) and references therein. During a global dust storm, the lower atmosphere

685   becomes dusty, and this dust load increases the energy absorption from the Sun, which increases

686   the neutral temperature of the lower atmosphere. The heated atmosphere then expands and gets

687   redistributed vertically, such that the neutral density increases in the thermosphere. Maxima in

688   the neutral density of the upper atmosphere correspond to maxima in the peak altitude. Withers

689   et al. (2015) found that both the top of the ionosphere and the peak altitude move up and then

690   down in altitude (by a few tens of km for the top of the ionosphere and a few km for the peak

691   altitude), as the global dust storms grow and then decay. In analogy, we think there is a possible

692   heating source (which we discuss later on), localized in areas of near vertical crustal fields which

693   may locally alter the vertical distribution of the ionizable neutral atmosphere and cause

694   subsequent raises of the altitude of the density profiles (without affecting the peak densities),

695   such as we observe in the series of altitude profiles. Both mechanisms mentioned earlier (neutral

696 atmosphere expansion and ionospheric plasma diffusion) may then simultaneously operate in the

697 regions of near vertical fields, such as to produce density structures in the entire altitude range of

698 the topside ionosphere.

699   The density structures reoccur in the same areas of magnetic anomalies on the dayside

700 (Andrews et al., 2014), no matter the field lines being closed or open, even in the absence of

701 solar wind entries, indicating that that their formation does not require magnetic reconnection

702 between the IMF and the magnetic anomalies (e.g. Diéval et al., 2015). We note that field-

703 aligned diffusion indeed occurs whatever the field lines are open or closed. Furthermore a

704 heating source may further enhance the density structures by either causing an expansion of the

705 neutral atmosphere (a given electron density level will rise in altitude) or by increasing the

706 electron temperature leading to reduced recombination rates and thus larger plasma densities

707 (Andrews et al., 2014). Diéval et al. (2015) based on their observations rejected the hypothesis

708 that the dayside bulges are primarily driven by ionization/heating input from precipitating solar

709 wind electrons, which had been proposed by earlier studies (Andrews et al., 2014, and references

710 therein). However, solar wind precipitation and other processes may still contribute to strengthen

711 existing density structures, as we will see below.

712   The status of the density structures changes as the planet rotates. The plasma density

713 decreases due to electron-ion recombination when it enters the shadow. The nightside densities

714 are often below 5000 cm^{-3} (the lowest densities detectable by MARSIS AIS), so in practice

715 seldom detectable (Němec et al., 2010). However, Němec et al. (2011b) have reported

716 intermittent observations of elevated electron peak densities in areas of near radial crustal fields

717 with frequent open-field line topology during nighttime. They were detected via oblique echoes,

718 indicating that these density structures were inclined plasma layers. Diéval et al. (2014) found

719   that such cases of high peak densities on nightside tend to be observed simultaneously with

720   precipitating tens to hundreds eV electrons (auroral or magnetotail), above the strong magnetic

721   anomalies of the Southern hemisphere, at times when the IMF points Westward. Additional

722   heating and ionization by energetic electron entries was thus necessary for the densities to

723   become large enough to become detectable by MARSIS (Diéval et al., 2014; Němec et al.,

724   2011b). Diéval et al. (2015) postulated that a recurrent process independent from external

725   conditions causes the density structures to reform during daytime in areas of near radial crustal

726   fields, and thereafter they would disappear during nighttime due to plasma densities becoming

727   too low to be measured. These authors suggested that these structures would be sporadically

728   enhanced at times of energetic electron precipitation driven by external conditions, making them

729   observable by MARSIS. The observations reported here imply that this recurrent process

730   involves transport (of plasma and/or of neutrals).

731   In general, the dayside electron densities at altitudes > 300 km are greater in areas of

732   crustal fields than in areas without (e.g. Andrews et al., 2013; 2015). At these high altitudes, the

733   ionosphere is in the transport regime. This difference may occur due to a facilitated vertical

734   transport of plasma along near vertical crustal field lines, while such vertical transport is

735   inhibited in areas where the interplanetary magnetic field (nearly horizontal orientation on

736   dayside, e.g. Brain et al., 2003) is free to permeate low altitudes. At the same time, the planetary

737   plasma is trapped within the mini-magnetospheres (e.g. Ramstad et al., 2016), where the solar

738   wind seldom has access and can thus not trigger ion loss, which keeps plasma densities high.

739   Similarly, plasma scale heights were found to be larger at 200 - 250 km altitudes, than at 150 -

740   200 km altitudes, in areas of near-radial crustal fields, due to the facilitated upward diffusion of

741   plasma along the field lines (e.g. Ness et al., 2000).

There have been reports of sporadically elevated peak densities in areas of near radial crustal fields on the dayside (Duru et al., 2016; Fallows et al., 2016, presented at DPS meeting #48; Nielsen et al., 2007b). We note that they are not necessarily related to the (recurrent) formation of density structures, but may happen simultaneously and enhance the structures further. Nielsen et al. (2007b) found no simultaneous observations of precipitating plasma/X-ray flux able to explain cases of high densities at low altitude. They invoked the reduction of the electron-ion recombination rate due to Joule heating of atmospheric neutrals by AC electric fields related to plasma instabilities in areas of open crustal field lines. Finally, Duru et al. (2016) have observed, in an area of strong near vertical crustal fields, a dayside case with simultaneous detection of: local plasma depletion at spacecraft altitude, peak density enhancement, and oblique echoes. They postulated that an earlier instance of magnetic reconnection between the crustal fields and the IMF allowed accelerated precipitating electrons to reach low altitudes along open field lines, providing heating and ionization which may have strengthened a density structure already present, and at the same time driving energization and outflow of planetary ions such as to form a density cavity at high altitude. They suggested that the increased peak electron density may have been caused by either the Nielsen et al. (2007b) mechanism or the electron precipitation.

We note that although the dayside oblique echoes are commonly observed above magnetic anomalies, plasma depletions and peak density enhancements are on the other hand rarely observed during daytime (Duru et al., 2016; Fallows et al., 2016, presented at DPS meeting #48; Hall et al., 2016). On the dayside, enhanced peak densities are found in areas of near radial fields being more often open than usual and can be detected via oblique echoes (Fallows et al., 2016, presented at DPS meeting #48), similar to their nightside counterparts

765 (Němec et al., 2011b). From the Duru et al. (2016) case, we infer that whatever the shape

766 distribution of the target of oblique echoes was when it formed, sporadic processes appear to

767 have altered its shape distribution into: presumably a dip at MEX location and a bulge near the

768 ionospheric peak.

769   The methodology of the present work focuses on the study of time series of EDPs at

770 selected frequencies, to study horizontal density gradients. Another interesting way to study the

771 topside ionosphere is to examine the vertical structure of the ionosphere, with single EDPs

772 obtained either by inversion of ionograms or by radio occultation technique, to identify vertical

773 density gradients (e.g. Kopf et al., 2008; Withers et al., 2005).

774   Withers et al. (2005) observed that density bumps and bite-outs can exist in regions of

775 strong magnetic anomalies and that their occurrence seemed to depend on the crustal field

776 inclination and azimuth. The altitudes of these features were found within the dynamo region of

777 the Martian ionosphere, which exists between 120 and 190 km altitude for a magnetic field

778 strength of 100 nT, as estimated by Withers et al. (2005). These authors suggested the role of

779 neutral winds, magnetic field, and ionized plasma, within the dynamo region, to generate

780 induced ionospheric currents and associated magnetic fields, which could modify the density

781 profiles such as to create bite-outs or bumps. Field-aligned currents and Pedersen currents in

782 magnetic cusp areas were simulated by e.g. Fillingim et al. (2010, 2012); Riousset et al. (2013,

783 2014). Such currents are expected to always be present, and can be a recurrent source of heating

784 of the neutral atmosphere, localized to regions of magnetic cusps. Heating at altitudes below the

785 ionospheric peak, could cause the typically higher altitudes we have observed for the entire

786 topside ionosphere in these regions.

787   Kopf et al. (2008) have discovered the existence of transient topside layers above the

788   main ionospheric peak, at typical altitudes 180-240 km on the dayside, with an occurrence rate

789   decreasing when going from the subsolar region to the terminator (from 60% to 5% of

790   observation time). The topside layers are found mostly in regions of low crustal magnetic field

791   strength (e.g. Kim et al., 2012, Kopf et al., 2017). It is not known whether topside layers exist in

792   regions of stronger crustal fields, because the presence of electron cyclotron harmonics in the

793   ionograms can hinder the visibility of the ionospheric traces at low frequency, including any

794   potential topside layer. Concurrent measurements of topside layers by MARSIS onboard the

795   MEX orbiter and by the in-situ particle and field package onboard the MAVEN orbiter indicate

796   localized increases in the in-situ electron density and total ion density in the vicinity of the

797   topside layers detected remotely by MARSIS (Kopf et al., 2017). These authors also found

798   simultaneous magnetic field rotations and magnetic field dips, attributed to current sheets.

799   We remark that these topside layers have two characteristics which are incompatible with

800   the characteristics of the density structures investigated in the present work: the former are

801   transient and are detected away from regions of significant crustal fields (but could possibly exist

802   in such regions although non detectable due to cyclotron harmonics), while the latter reoccur

803   regularly and only above regions of significant crustal fields. In addition, the former have been

804   attributed to various mechanisms involving the solar wind interaction with the topside

805   ionosphere (e.g. Kopf et al., 2017), while the latter seem to have no relationship to the upstream

806   solar wind conditions or to the presence/absence of magnetosheath plasma entries at MEX

807   altitude (e.g. Andrews et al., 2014, Diéval et al., 2015). Therefore there seems to be no link

808   between the topside layers and the regions giving oblique echoes. Another indication that these

809   ionospheric features are independent is that topside layers can be present and give oblique echoes

810   if found in areas where the main ionosphere layer already gives oblique echoes, but are not

811   present otherwise (Venkateswara Rao et al., 2017).

812   Bulges may be the primary type of density structure to appear, as modelled in the simple

813   case of vertical diffusion by Matta et al. (2015). They are the most observed simplest shape.

814   Other shapes likely require more complex conditions. The formation of slopes may be related to

815   gradients in the ability of the plasma to be transported, favoring convex slopes or concave slopes

816   depending on circumstances. Dips possibly form as a result of ion outflow along open field lines

817   at occasions of magnetic reconnection between the IMF and the crustal fields, during which the

818   solar wind is able to energize the planetary ions within the mini-magnetosphere. It is also

819   possible that a magnetic arcade near the terminator possesses one footprint on dayside and the

820   other footprint on nightside, such that electrons produced on dayside are lost on nightside after

821   travelling along the arcade (e.g. Xu et al., 2016): this may cause a dip within the illuminated area

822   of near-radial field lines. The restriction of our study to SZA $< 85°$ certainly limits the

823   observation of this situation. Instead we are working here with the commonly observed dayside

824   events where both footprints of the corresponding magnetic arcades are reasonably expected to

825   be illuminated. A decrease of the altitude level at selected frequencies could also be brought by

826   the contracting and cooling of the underlying atmosphere, after a transient heating source (such

827   as from solar wind precipitation) has subsided.

828

829   5) Summary

830   This paper reports a statistical study of oblique ionospheric echoes in the dayside Martian

831   ionosphere identified with the MARSIS AIS radar data. The reflecting targets for these oblique

832 echoes are non-horizontal localized electron density structures associated to regions of near

833 radial crustal magnetic fields. The altitude variations (shape) of 48 density structure events

834 corrected for signal dispersion have been investigated through time series of EDPs, by

835 comparing a reference EDP (PI EDP) to the other EDPs in the same time series. We obtained the

836 following results:

837 1.   The altitude differences between the PI EDP and the edge EDPs tend to be larger at low

838 frequencies (high altitudes) and smaller at high frequencies (low altitudes), with values going

839 from a few tens of km down to a few km as frequency increases (equivalently altitude

840 differences of a few tens of % down to a few % relative to the altitude of the PI EDP). The

841 density structures are found with large altitude variations in the region of transport regime (above

842 ~200 km altitude), and with smaller altitude variations in the region of photochemistry regime

843 (below ~200 km altitude).

844 2.   The inspection of the hyperbola signatures in echograms at selected frequencies indicates

845 that oblique echoes are more developed at low frequency than at high frequency, which is

846 consistent with the altitude differences between PI EDP and edges EDPs to be larger (more tilted

847 density contour) at low frequency than at high frequency, and agrees with the result from Nielsen

848 et al. (2007a).

849 3.   There are four simplest possible shapes for inclined structures able to give oblique

850 echoes: bulge, dip, uphill slope and downhill slope. Uphill slopes and downhill slopes can be

851 concave or convex. Convex slope events resemble dips (downward swell) and concave slope

852 events resemble bulges (upward swells).

853   4.   A given event may keep the same shape over all frequencies or change shape over

854   frequency. The changes of shape over frequency are gradual, but systematic, with natural

855   transitions between bulge and dip, separated by concave and convex slope events in the right

856   order.

857   5   The comparison of the time series of EDPs at selected frequencies with the 1.8 - 2 MHz

858   integrated echograms for individual events brings intriguing results. The apparent altitude of the

859   apex of the hyperbola signature in the echograms does not vary consistently with the altitude

860   levels corrected for dispersion: the apex of the hyperbola does not necessarily correspond to the

861   highest (or lowest) real altitude level in the time series. The presence of one or two clear legs or

862   short/unclear legs in the hyperbola signature does not seem to relate to the simplest shape in the

863   EDP time series (it may be any of these: bulge, dip, downhill and uphill slopes).

864   6.   In most of the frequency range of the EDPs, the number of bulges dominates the numbers

865   of other shapes. The number of bulges peaks at a fixed frequency 2.111 MHz, much higher than

866   for the other shapes: the numbers of uphill slopes, downhill slopes and dips peak at a fixed

867   frequency of 1.63, 1.455, and 1.52 MHz, respectively.

868   7.   At a given frequency, the altitude differences between the PI EDP and the edge EDPs tend

869   to be larger in absolute value for bulges than for other shapes. It is possible that the smaller

870   altitude differences of uphill slope, downhill slope and dip events could be a bias from their

871   small numbers. The median altitude difference we have determined for bulges at a fixed

872   frequency 1.848 MHz is 12.4 km, which is of the same order as the rms apparent altitude of 19

873   km at a fixed frequency 1.8 MHz reported by Duru et al. (2006).

874   8.   The examination of the entire frequency range of the EDPs in the time series of individual

875   events indicates the possible presence of topside layers, density bumps and density bite-outs (e.g.

876   Kopf et al., 2008, Withers et al., 2005) in the form of slight ledges in the vertical structure. Also,

877   the altitude level at a fixed frequency 1.936 MHz clearly increases when the ionospheric peak

878   altitude increases, and has a weak increasing trend when the peak density increases. The entire

879   topside ionosphere seems to move up and down in areas giving oblique echoes.

880   9.   The latitude extension of the areas giving oblique echoes, which is usually comparable to

881   the latitude extension of the corresponding magnetic cusps, permits a sampling of a wide range

882   of crustal field orientations, from near-vertical up to near-horizontal. There is a tendency for

883   more vertical crustal fields toward the center of the density structures, and more horizontal fields

884   toward the edges.

885   10.   At a fixed frequency 1.936 MHz, the relative altitude differences between the PI EDP and

886   the other EDPs in the time series of individual events, and the classification into the 4 possible

887   simplest shapes, seem to be independent or weakly dependent upon the crustal field orientation,

888   and vary for events located in geographical proximity (within 10° longitude) but detected at

889   different dates and times.

890   Transport appears to be a key element in the formation of density structures. Two

891   recurrent mechanisms based on transport could operate, possibly at the same time: 1) field-

892   aligned diffusion of plasma along near radial (open or closed) field lines, 2) electron density

893   levels rising in altitude through the expansion of the ionizable neutral atmosphere presumably

894   due to localized Joule heating by ionospheric currents at magnetic cusps. Other mechanisms may

895   alter the density structures either by enhancing them or weakening them. Heating/ionization by

896 electron precipitation or AC electric fields may further increase the plasma densities in areas of

897 near-radial open crustal fields.

898 In-situ measurements in the altitude range of the density structures would be a valuable

899 complement to the remote measurements enabled by MARSIS AIS. In particular, future studies

900 making use of the rich combined capabilities of Mars Express and MAVEN would help

901 understand the formation and evolution of individual structures, in particular, more in-situ

902 measurements of downhill slopes, uphill slopes and dips are needed. Future studies also need to

903 evaluate ray tracing of radio signals through models of ionospheric layers to study the

904 characteristics of oblique echoes; they would also be very useful to understand the intriguing

905 results brought by the comparison of EDP time series and echograms.

906

907 Appendix A

908 The derived altitude profiles of Morgan et al. (2013) make two assumptions: vertical

909 propagation and plane parallel stratification. Here we discuss potential issues in applying these

910 assumptions in regions of density structures. Morgan et al. (2013) warned about the use of the

911 profiles in the areas of oblique echoes, because the assumption of vertical propagation may not

912 be true. In fact the single ionospheric echo received may be vertical or oblique depending on the

913 density layer inclination at the reflection point. We note that MARSIS measures only the time

914 delay to receive the echo, without knowledge of the angle between the echo direction and the

915 nadir. This time delay is given as input to the inversion routine, which outputs the range

916 corrected for dispersion. The inversion itself does not need the direction of the echo. It is only

917 afterwards, at the stage of calculating the altitude of the obtained profile that the assumption of

918   vertical propagation is made: layer altitude = MEX altitude – layer range. Given that the

919   reflection angle cannot be known, it is not possible to account for this angle to amend the layer

920   altitude. Thus in practice we can only use the altitudes as derived with the nadir echo

921   assumption. On the other hand, the assumption of plane parallel stratification is applied inside

922   the inversion routine and is thus required at an early stage to produce a range corrected for

923   dispersion. Given the trend of the altitude differences PI EDP – edge EDP to increase over

924   frequency (Figure 7), one may then wonder whether the density structures still respect a plane

925   parallel stratification over their whole frequency range. Below we check the validity of these two

926   assumptions, for the events in our list, by using information from the Results Section.

927   We want to determine the angle that the inclined layer makes with the horizontal for

928   different frequencies by considering a line joining the PI altitude and the edge altitude (beginning

929   or end), and the angle between such successive inclined layers of consecutive frequencies. We

930   care about how large the angles are, so we take their absolute values. In practice, it means

931   changing all the events into bulges (absolute value of altitude differences for both edges), which

932   is good for our purpose, especially since the majority of the events are bulges. Then we simplify

933   the shape of the structures by keeping only the altitude variations of the edge EDPs and the PI

934   EDP, ignoring the profiles in between, which effectively turns the shapes into triangles. Finally

935   we can calculate, for each frequency f, the angle α_f between a horizontal line at the altitude of

936   the edge point and a line joining the altitudes of the edge and PI points: $\tan \alpha_f = H_f/D$. Here

937   H_f is the absolute value of the altitude difference PI EDP – edge EDP at frequency f and D is the

938   horizontal distance traveled by MEX between the edge and PI times (using the MEX velocity

939   and the absolute value of the time difference between edge and PI). This is done separately for

940   the beginning and end edges. Then we deduce the angle $\theta_{f2\,f1}$ between two successive inclined

941   density layers of consecutive frequencies $f1$ and $f2$ ($f2 > f1$) as $\theta_{f2\,f1} = \alpha_{f2} - \alpha_{f1}$.

942   Remark: the density layer is very likely to be horizontal or near horizontal both at the edge point

943   (because it is very close to the surrounding normal ionosphere) and at the PI point (especially for

944   a bulge or a dip), so we can use these altitude values directly, with the nadir echo assumption.

945   Figure A1 shows the distributions of the angle α_f (panel a) and the angle $\theta_{f2\,f1}$ (panel b),

946   as a function of frequency, for all the events, for both the beginning and end edges, plotted as

947   grey dots. The red dots correspond to the median angles versus frequency. Since α_f is

948   proportional to H_f, the angle between horizontal and inclined layer tends to increase when the

949   frequency decreases (panel a), just like the altitude difference does increase. The distribution of

950   angles broadens as frequency decreases, the angle increases from a few degrees at high

951   frequency, up to ~15° at low frequency, confirmed by the increasing trend of the median values

952   from 3.4 to 4.5°. Therefore, for these events, the inclined layers from the edge point to the PI

953   point are weakly inclined to the horizontal, with angles typically small at all frequencies. Then,

954   the distribution of $\theta_{f2\,f1}$ does not vary over frequency (panel b), remaining close to zero at all

955   frequencies: the angles between successive layers vary mostly up to 0.5°, with the median values

956   remaining $\leq 0.1°$. Therefore these density layers are making negligible angles to each other at all

957   frequencies, and basically appear as parallel strata from the edge point to the PI point. We

958   conclude that for our list of density structures, the assumption of plane parallel stratification is

959   certainly valid, and the assumption of vertical reflection is, although no exactly true, good

960   enough as approximation. Therefore we are confident that these EDPs are valid and provide

961   useful insight for these particular density structures.

For comparison, Nielsen et al. (2007a) estimated the angles of inclined layers to the vertical for a few cases of density structures, with a different hypothesis (assuming a fixed altitude for the reflection point), and found a wide range of values from 5 to 90°. We note that the assumption of vertical propagation is certainly not applicable for strongly inclined structures, and thus the vertical profiles would be invalid in this case.

References:

Acuña, M. H., et al. (1999), Global distribution of crustal magnetization discovered by the Mars Global Surveyor MAG/ER experiment, *Science*, 284(5415), 790–793, doi:10.1126/science.284.5415.790

Andrews, D. J., et al. (2013), Determination of local plasma densities with the MARSIS radar: Asymmetries in the high-altitude Martian ionosphere, *J. Geophys. Res*., 118, 6228–6242, doi:10.1002/jgra.50593

981   Andrews, D. J., et al. (2014), Oblique reflections in the Mars Express MARSIS data set: Stable

982   density structures in the Martian ionosphere, *J. Geophys. Res.*, 119, 3944–3960,

983   doi:10.1002/2013JA019697

984   Andrews, D. J., et al. (2015), Control of the topside Martian ionosphere by crustal magnetic

985   fields, *J. Geophys. Res.*, 120, 3042–3058, doi:10.1002/2014JA020703

986   Barabash, S., et al. (2006), The Analyzer of Space Plasmas and Energetic Atoms (ASPERA-3)

987   for the Mars Express Mission, *Space Sci. Rev.*, 126(1–4), 113–164, doi:10.1007/s11214-006-

988   9124-8

989   Brain, D. A., et al. (2003), Martian magnetic morphology: Contributions from the solar wind and

990   crust, J. Geophys. Res., 108(A12), 1424, doi:10.1029/2002JA009482

991   Brain, D. A., et al. (2007), Electron pitch angle distributions as indicators of magnetic field

992   topology near Mars, *J. Geophys. Res.*, 112, A09201, doi:10.1029/2007JA012435

993   Budden, K. G. (1961), Radio Waves in the Ionosphere, Cambridge Univ. Press, Cambridge, U. K

994   Cain, J. C., et al. (2003), An n = 90 internal potential function of the Martian crustal magnetic

995   field, *J. Geophys. Res.*, 108(E2), 5008, doi:10.1029/2000JE001487

996   Diéval, C., et al. (2014), MARSIS observations of the Martian nightside ionosphere dependence

997   on solar wind conditions, *J. Geophys. Res.*, 119, 4077–4093, doi:10.1002/2014JA019788

998   Diéval, C., et al. (2015), MARSIS remote sounding of localized density structures in the dayside

999   Martian ionosphere: A study of controlling parameters, *J. Geophys. Res.*, 120, 8125–8145,

1000 doi:10.1002/2015JA021486

1001   Duru, F., et al. (2006), Magnetically controlled structures in the ionosphere of Mars, *J. Geophys.*

1002   *Res.*, 111, A12204, doi:10.1029/2006JA011975

1003   Duru, F., et al. (2010), Overlapping ionospheric and surface echoes observed by the Mars

1004   Express radar sounder near the Martian terminator, *Geophys. Res. Lett.*, 37, L23102,

1005   doi:10.1029/2010GL045859

1006   Duru, F., et al. (2016), A case study of a density structure over a vertical magnetic field region

1007   in the Martian ionosphere, *Geophys. Res. Lett.*, 43, 4665–4672, doi:10.1002/2016GL068686

1008   Fallows, K., et al. (2016), Oblique echoes at unusually high frequencies in MARSIS-AIS

1009   measurements of the topside ionosphere of Mars, American Astronomical Society, DPS meeting

1010   #48, id.220.33

1011   Fillingim, M. O., et al. (2010), Localized ionization patches in the nighttime ionosphere of Mars

1012   and their electrodynamic consequences, *Icarus*, 206(1), 112–119,

1013   doi:10.1016/j.icarus.2009.03.005

1014   Fillingim, M. O., et al. (2012), On wind-driven electrojets at magnetic cusps in the nightside

1015   ionosphere of Mars, *Earth Planets Space*, 64(2), 93–103, doi:10.5047/eps.2011.04.010

1016   Fox, J. L., and K. E. Yeager (2006), Morphology of the near-terminator Martian ionosphere: A

1017   comparison of models and data, *J. Geophys. Res.*, 111, A10309, doi:10.1029/2006JA011697

1018   Gurnett, D. A., et al. (2005), Radar soundings of the ionosphere of Mars, *Science*, 310(5756),

1019   1929–1933, doi:10.1126/science.1121868

Hall, B. E. S., et al. (2016), A survey of superthermal electron flux depressions, or "electron holes," within the illuminated Martian induced magnetosphere, *J. Geophys. Res*., vol. 121(5), 4835–4857, doi: 10.1002/2015JA021866

Hantsch, M. H., and Bauer S. J. (1990), Solar control of the Mars ionosphere, *Planetary and Space Science*, vol. 38, 539-542, doi: 10.1016/0032-0633(90)90146-H.

Kim, E., et al. (2012), The Analysis of the Topside Additional Layer of Martian Ionosphere Using MARSIS/Mars Express Data, *J. Astron. Space Sci*., 29(4), 337-342, doi: 10.5140/JASS.2012.29.4.337

Kopf, A. J., et al. (2008), Transient layers in the topside ionosphere of Mars, *Geophys. Res. Lett*., 35, L17102, doi:10.1029/2008GL034948

Kopf, A. J., et al. (2017), The transient topside layer and associated current sheet in the ionosphere of Mars*, J. Geophys. Res*., 122, 5579–5590, doi:10.1002/2016JA023591

Matta, M., et al. (2015), Interpreting Mars ionospheric anomalies over crustal magnetic field regions using a 2-D ionospheric model, *J. Geophys. Res*., 120, 766–777, doi:10.1002/2014JA020721

Morgan, D. D., et al. (2008), Variation of the Martian ionospheric electron density from Mars Express radar soundings, *J. Geophys. Res*., 113, A09303, doi:10.1029/2008JA013313

Morgan, D. D., et al. (2013), The processing of electron density profiles from the Mars Express MARSIS topside sounder, *Radio Sci*., 48, 197–207, doi:10.1002/rds.20023

Nagy, A., et al. (2004), The plasma Environment of Mars, *Space Sci. Rev*., 111(33), doi:10.1023/B:SPAC.0000032718.47512.92

1041 Němec, F., et al. (2010), Nightside ionosphere of Mars: Radar soundings by the Mars Express
1042 spacecraft, *J. Geophys. Res.*, 115, E12009, doi:10.1029/2010JE003663

1043 Němec, F., et al. (2011a), Dayside ionosphere of Mars: Empirical model based on data from the
1044 MARSIS instrument, *J. Geophys. Res.*, 116, E07003, doi:10.1029/2010JE003789

1045 Němec, F., et al. (2011b), Areas of enhanced ionization in the deep nightside ionosphere of
1046 Mars, *J. Geophys. Res,* vol. 116, E06006, doi:10.1029/2011JE003804

1047 Němec, F., et al. (2016a), On improving the accuracy of electron density profiles obtained at
1048 high altitudes by the ionospheric sounder on the Mars Express spacecraft, *J. Geophys. Res.*, 121,
1049 10,117–10,129, doi:10.1002/2016JA023054

1050 Němec, F., et al. (2016b), Empirical Model of the Martian Dayside Ionosphere: Effects of
1051 Crustal Magnetic Fields and Solar Ionizing Flux at Higher Altitudes, *J. Geophys. Res.*, 121,
1052 1760-1771, doi: 10.1002/2015JA022060

1053 Ness, N. F., et al. (2000), Effects of magnetic anomalies discovered at Mars on the structure of
1054 the Martian ionosphere and solar wind interaction as follows from radio occultation experiments,
1055 *J. Geophys. Res.*, vol. 105(A7), 15991-16004, doi: 10.1029/1999JA000212

1056 Nielsen, E., et al. (2007a), Vertical sheets of dense plasma in the topside Martian ionosphere, *J.*
1057 *Geophys. Res.*, 112, E02003, doi:10.1029/2006JE002723

1058 Nielsen, E., et al. (2007b), Local plasma processes and enhanced electron densities in the lower
1059 ionosphere in magnetic cusp regions on Mars, vol. 55(14), 2164–2172, doi:
1060 10.1016/j.pss.2007.07.003

1061 Picardi, G., et al. (2004), MARSIS: Mars Advanced Radar for Subsurface and Ionospheric

1062 Sounding, in Mars Express: A European Mission to the Red Planet, edited by A. Wilson, pp. 51–

1063 69, ESA Publ. Div., Noordwijk, Netherlands

1064 Ramstad, R., et al. (2016), Effects of the crustal magnetic fields on the Martian atmospheric ion

1065 escape rate, *Geophys. Res. Lett*., 43, 10,574–10,579, doi:10.1002/2016GL070135

1066 Riousset, J. A., et al. (2013), Three-dimensional multifluid modeling of atmospheric

1067 electrodynamics in Mars' dynamo region, *J. Geophys. Res*., 118, 3647–3659,

1068 doi:10.1002/jgra.50328

1069 Riousset, J. A., et al. (2014), Electrodynamics of the Martian dynamo region near magnetic cusps

1070 and loops, *Geophys. Res. Lett*., 41, 1119–1125, doi:10.1002/2013GL059130

1071 Sánchez-Cano, B., et al. (2016), Solar cycle variations in the ionosphere of Mars as seen by

1072 multiple Mars Express data sets, *J. Geophys. Res*., 121, 2547–2568, doi:10.1002/ 2015JA022281

1073 Venkateswara Rao, N., et al. (2017), Magnetically controlled density structures in the topside

1074 layer of the Martian ionosphere, *J. Geophys. Res*., 122(5), 5619-5629, doi:

1075 10.1002/2016JA023545

1076 Wang, J.-S., and E. Nielsen (2003), Behavior of the Martian dayside electron density peak during

1077 global dust storms, *Planetary and Space Science*, 51, 329 – 338, doi: 10.1016/S0032-

1078 0633(03)00015-1

1079 Wang, X.-D., et al. (2009), ''Hook'' structure in MARSIS ionogram and its interpretation,

1080 *Geophys. Res. Lett*., 36, L13103, doi: 10.1029/2009GL038844

1081   Withers, P., et al. (2005), Ionospheric characteristics above Martian crustal magnetic anomalies,

1082   *Geophys. Res. Lett.*, 32, L16204, doi:10.1029/2005GL023483

1083   Withers, P., et al. (2015), Recovery and validation of Mars ionospheric electron density profiles

1084   from Mariner 9, *Earth, Planets and Space*, 67-194, doi: 10.1186/s40623-015-0364-2

1085   Xu, S., et al. (2016), Deep nightside photoelectron observations by MAVEN SWEA:

1086   Implications for Martian northern hemispheric magnetic topology and nightside ionosphere

1087   source, *Geophys. Res. Lett.*, 43, 8876–8884, doi:10.1002/2016GL070527

1088

1089   Figures:

1090

1091
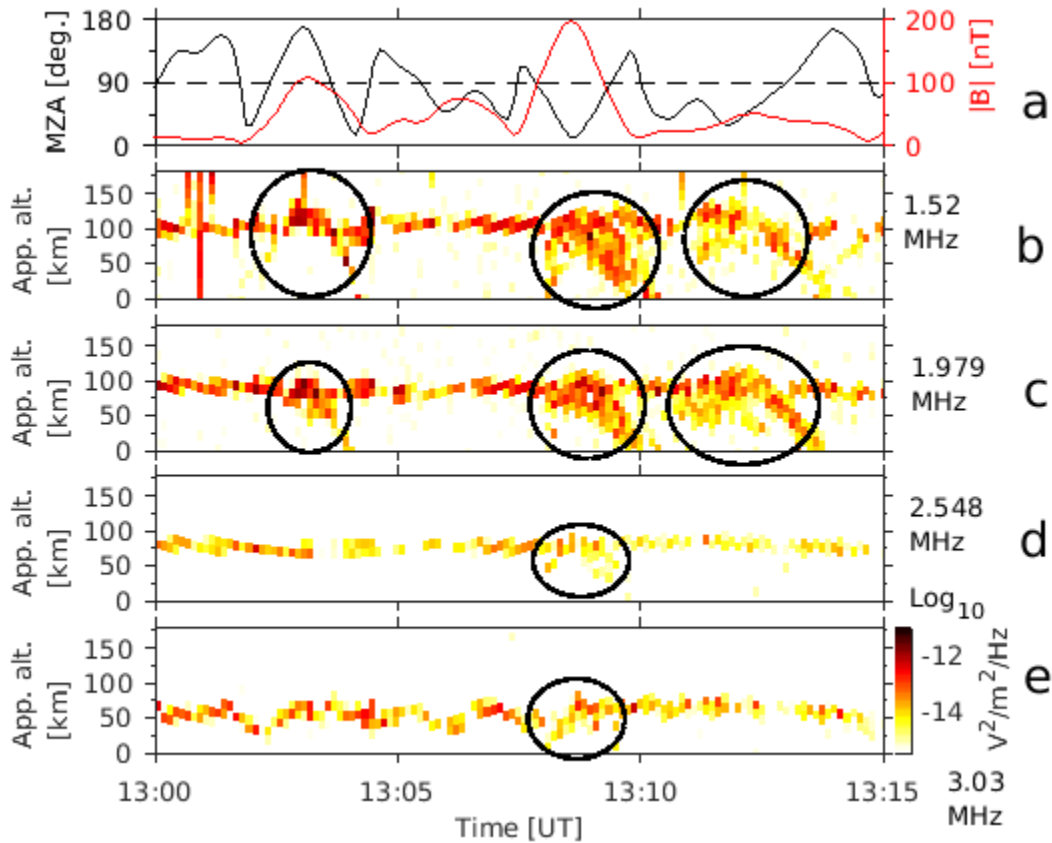
1092

Figure 1: Time series on 22 July 2006, 13:00-13:15 UT, orbit 3253. (a) Crustal magnetic field
calculated at 150 km altitude at MEX footprint using the Cain et al. (2003) model: magnetic
zenith angle (black curve, left axis) and magnetic field strength (red curve, right axis). The
horizontal black dashed line marks the 90° angle (horizontal orientation). (b) to (e) MARSIS
echograms at four sounding frequencies: 1.52 (b), 1.979 (c), 2.548 (d) and 3.03 MHz (e); the
vertical axis shows the apparent altitude and the color coding shows the received signal spectral
density. Black ellipses mark the hyperbola signatures associated to oblique echoes.

1100
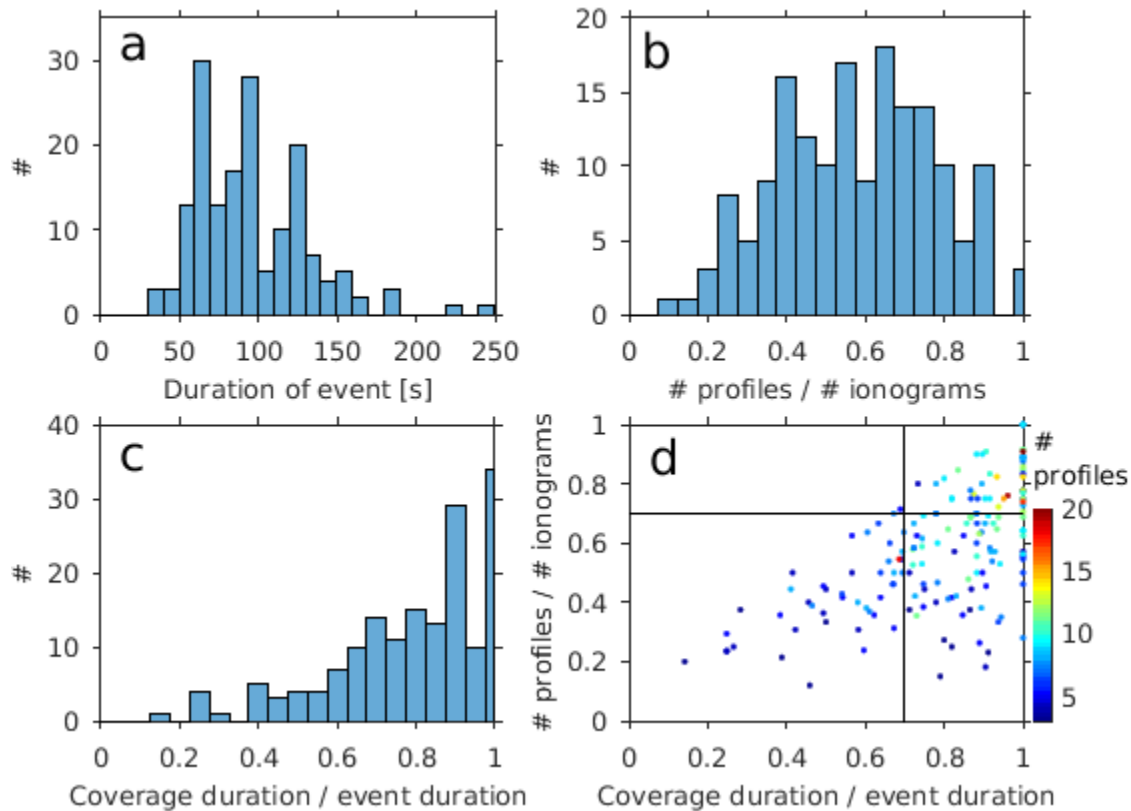
1101

Figure 2: (a) Distribution of event duration for all the events. (b) Distribution of the number of available EDPs divided by the number of ionograms during the duration of each event (ratio of numbers), for all the events. (c) Distribution of the duration of EDP coverage divided by the event duration of each event (ratio of durations), for all the events. (d) Scatter plot of the ratio of durations versus the ratio of numbers, colored by the number of available EDPs during the duration of each event, for all the events. Black solid vertical and horizontal lines are plotted for abscissa=0.7 and ordinate=0.7, respectively. We keep the 48 events for which: number of available EDPs divided by the number of ionograms ≥ 0.7 and duration of the EDP coverage divided by the event duration ≥ 0.7.

1112
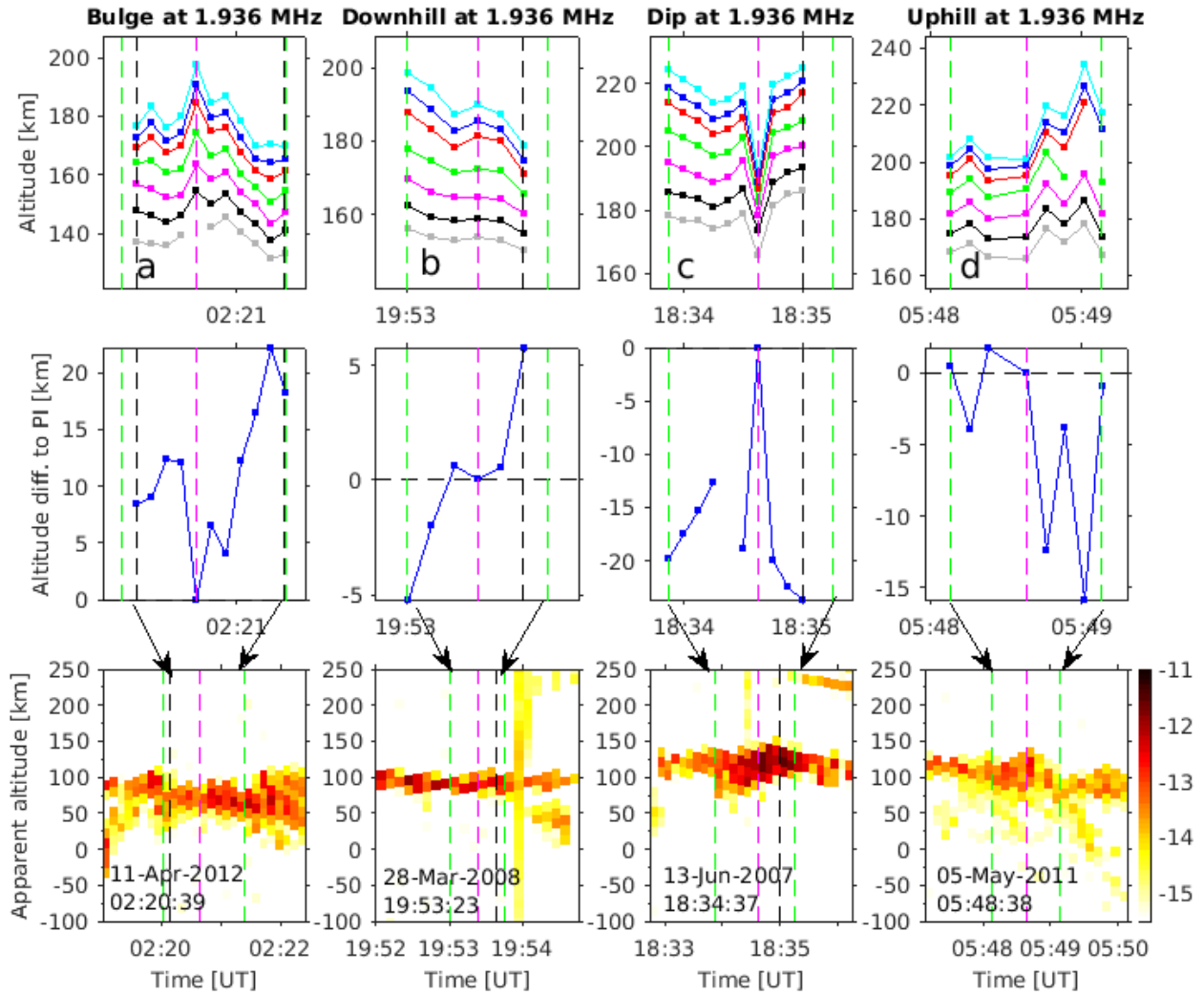
Figure 3: Examples of time series for four events. First column (a): bulge. Second column (b): downhill slope. Third column (c): dip. Fourth column (d): uphill slope. In all panels, the green vertical dashed lines mark the times selected for the beginning and end edges of the hyperbola signature; the black vertical dashed lines mark the times of the first and last available EDPs for the structure; the magenta vertical dashed line marks the time of PI EDP. First row: time series of available EDPs at different frequencies coded by color: 1.433 (cyan), 1.542 (blue), 1.651 (red), 1.848 (green), 2.067 (magenta), 2.286 (black) and 2.505 (grey) MHz, corresponding to 2.55×10^4, 2.95×10^4, 3.38×10^4, 4.23×10^4, 5.3×10^4, 6.48×10^4 and 7.78×10^4 cm^{-3}. The filled

1121 squares mark the measurement values of altitudes. Second row: time series of altitude difference

1122 between the PI EDP and each EDP, for the frequency level 1.936 MHz; values are zero for the PI

1123 EDP and for EDPs of identical altitude, positive for EDPs standing lower than the PI EDP,

1124 negative for EDPs standing higher than the PI EDP. The horizontal black dashed line marks

1125 altitude difference = 0. Third row: echograms integrated between 1.8-2 MHz, in the same format

1126 as in Figure 1. Notice the longer time scale shown, indicated by arrows. The date and time for

1127 the PI EDP of each event are indicated in the bottom row.

1128
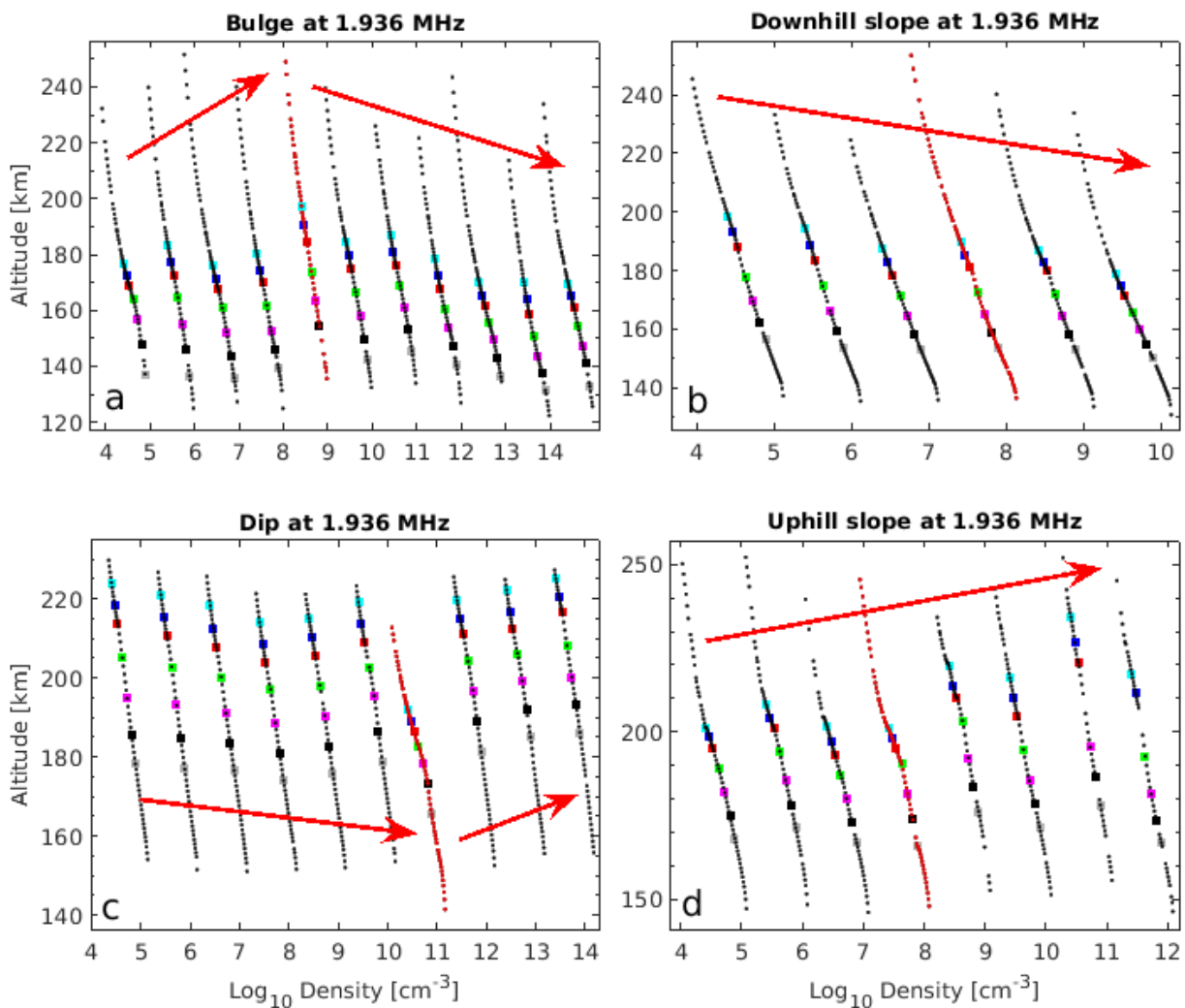
1129

1130 Figure 4: Series of EDPs for the same 4 events: (a) bulge, (b) downhill slope, (c) dip, (d) uphill

1131 slope. In each panel, the red curve is the PI EDP; the black curves are the other EDPs for the

1132 time series. The local frequency was excluded from analysis; the colored squares represent the

1133 same data points as in Figure 3 (same color coding for frequency). For each event, the EDPs are

1134 shown versus $\log_{10}$(density) in cm^{-3}, and the densities of the successive EDPs are multiplied by

1135 10^0, 10^1, 10^2, etc., for clarity. Red arrows are added to guide the eye.

1136
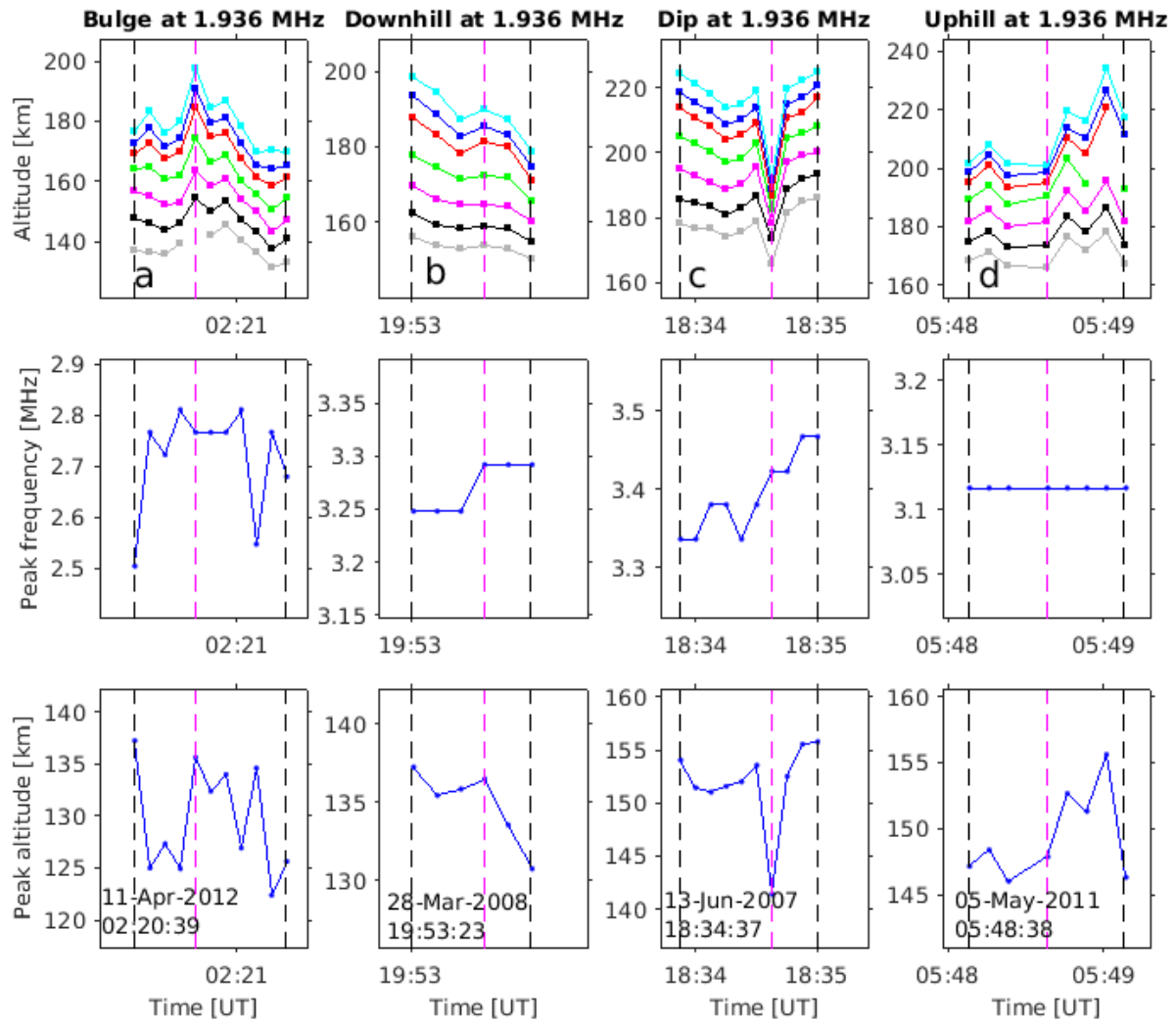
1137

1138 Figure 5: Examples of time series for the same 4 events. First column (a): bulge. Second column

1139 (b): downhill slope. Third column (c): dip. Fourth column (d): uphill slope. First row: almost

1140 same format as first row of Figure 3. Second row: time series of peak frequency. Third row: time

1141 series of peak altitude.
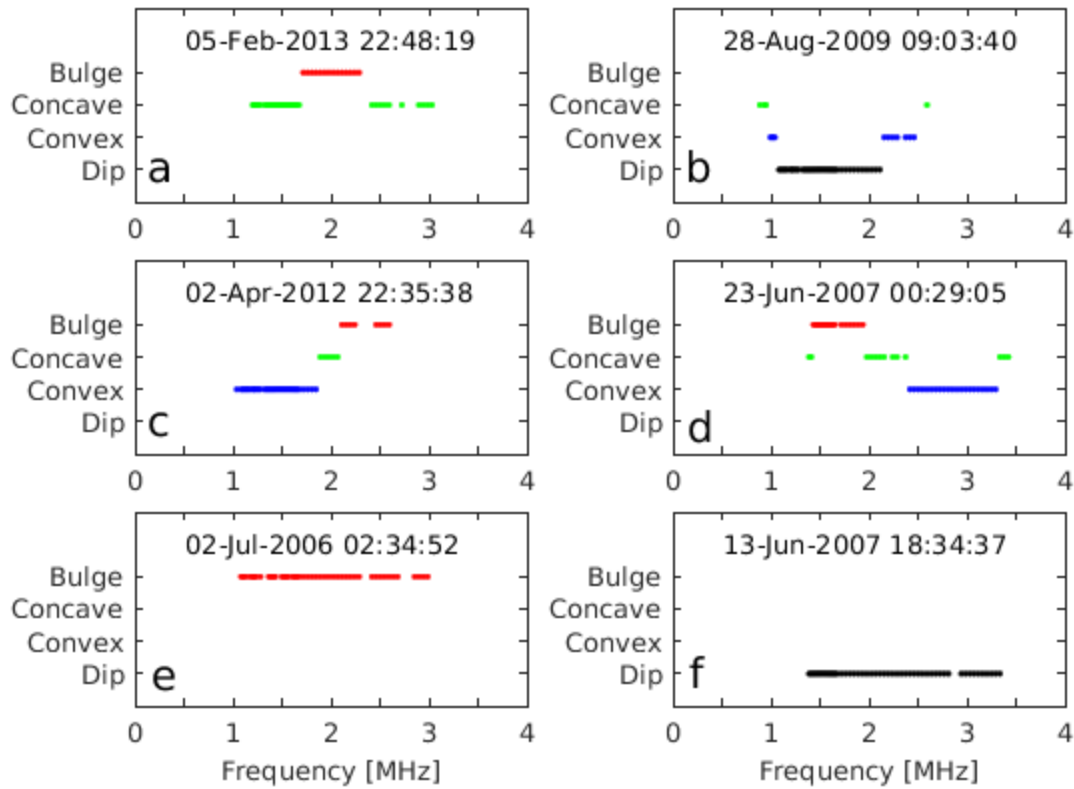
1142

1143 Figure 6: Examples of classification of the simplest shape of events as a function of frequency,

1144 for 6 events (date and time of PI EDP are indicated in each panel). The vertical axis displays the

1145 shape with corresponding colored dots: bulge (red), concave slope (green), convex slope (blue),

1146 dip (black). The local frequency was excluded from analysis.

1147

1148

1149
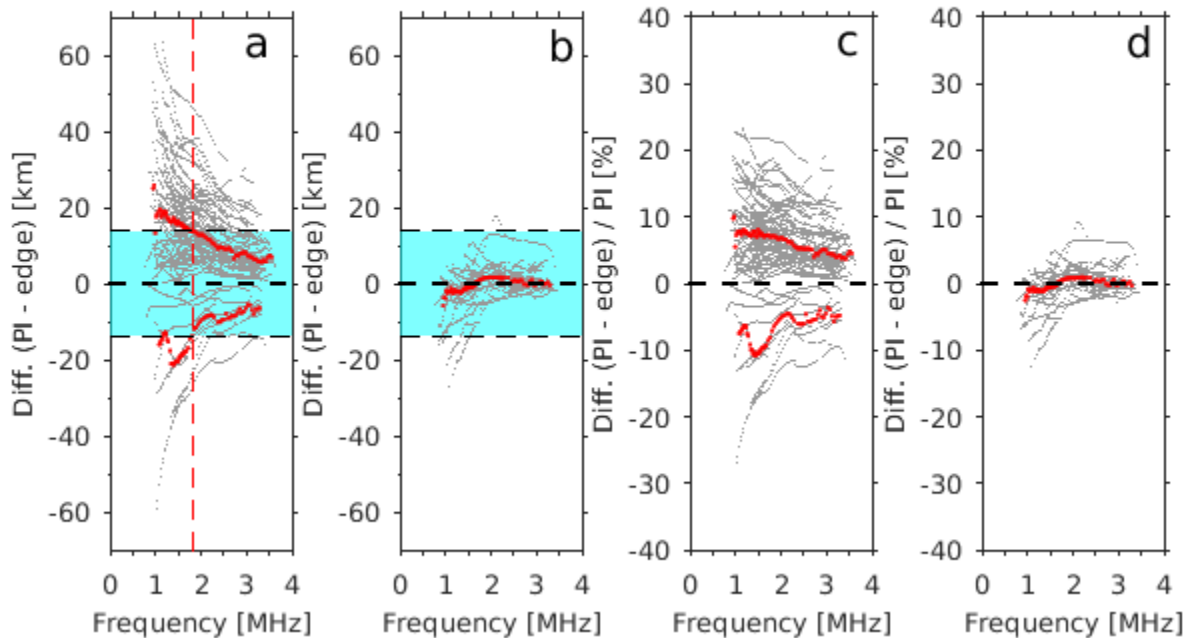
1150

Figure 7: (a,b) Altitude differences PI EDP – edge EDP (in km) for all the events as a function of

frequency, plotted as grey lines. (c,d) Altitude differences PI EDP – edge EDP relative to the

altitude of the PI EDP (%) for all the events as a function of frequency, plotted as grey lines. The

edge EDP refers to either the first EDP or the last EDP of the time series of each event. Altitude

differences which change sign over frequency are plotted in columns (b, d), while altitude

differences which keep either all-positive or all-negative over frequency are plotted in columns

(a, c). The local frequency was excluded from analysis. The red dots indicate the median of the

altitude differences as a function of frequency. In panels (a) and (c), the medians are shown

separately for the all-positive and the all-negative altitude differences. In panels (a,b), the thin

horizontal black dashed lines mark the 13.7 km and -13.7 km thresholds, and the regions with

abs(altitude difference) < 13.7 km are colored in cyan and the regions with abs(altitude

1162 difference) > 13.7 km are left in white, to help with clarity. In panel (a), the vertical red dashed

1163 line marks the threshold frequency 1.826 MHz (see text).

1164
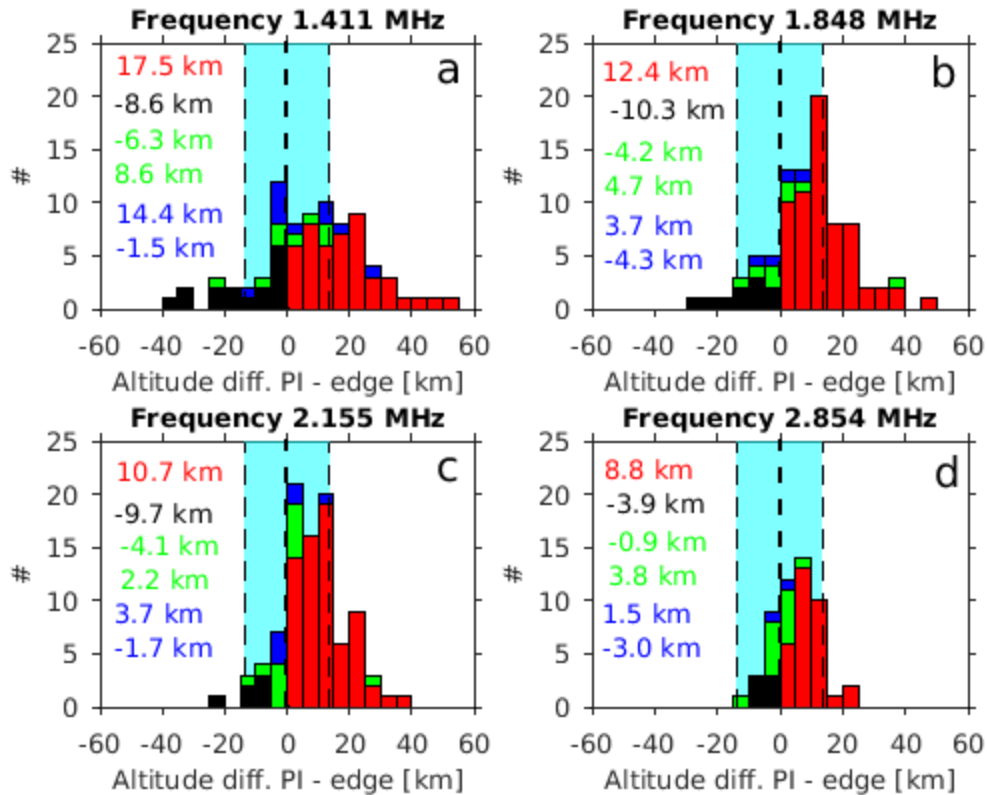
1165

1166 Figure 8: Distributions of altitude differences PI EDP – edge EDP of each event, for all the

1167 events, at 4 fixed frequencies: (a) 1.411, (b) 1.848, (c) 2.155 and (d) 2.854 MHz. The edge EDP

1168 is either the first or last EDP of the time series of an event. In each panel, the total distribution is

1169 separated into stacked color coded distributions for the 4 simplest shapes (same color code as

1170 Figure 6): bulge (red), dip (black), uphill slope (blue) and downhill slope (green). This means

1171 that in each bin, we count the number of events for each of the four event shapes and then trace

1172 colored bars stacked on top of each other; each bar corresponds to one event shape and its length

1173   is equal to the number of events. Thin vertical dashed black lines delimitate the regions of

1174   abs(altitude differences) < or > 13.7 km, with corresponding colored patches (cyan or white) for

1175   clarity. The median values of altitude differences for the different distributions are indicated in

1176   the panels with the same color code per type of shape.

1177
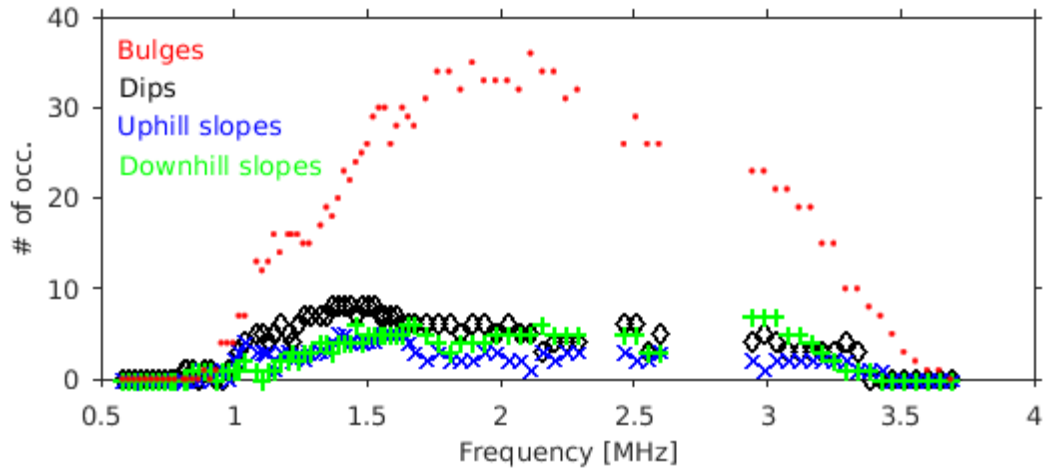
1178

1179   Figure 9: Distribution of the 4 simplest shapes as a function of frequency, for all the events,

1180   displayed as colored symbols, with the same color code as Figures 6 and 8: bulges (red dots),

1181   dips (black diamonds), uphill slopes (blue 'x'), downhill slopes (green '+'). Data points at

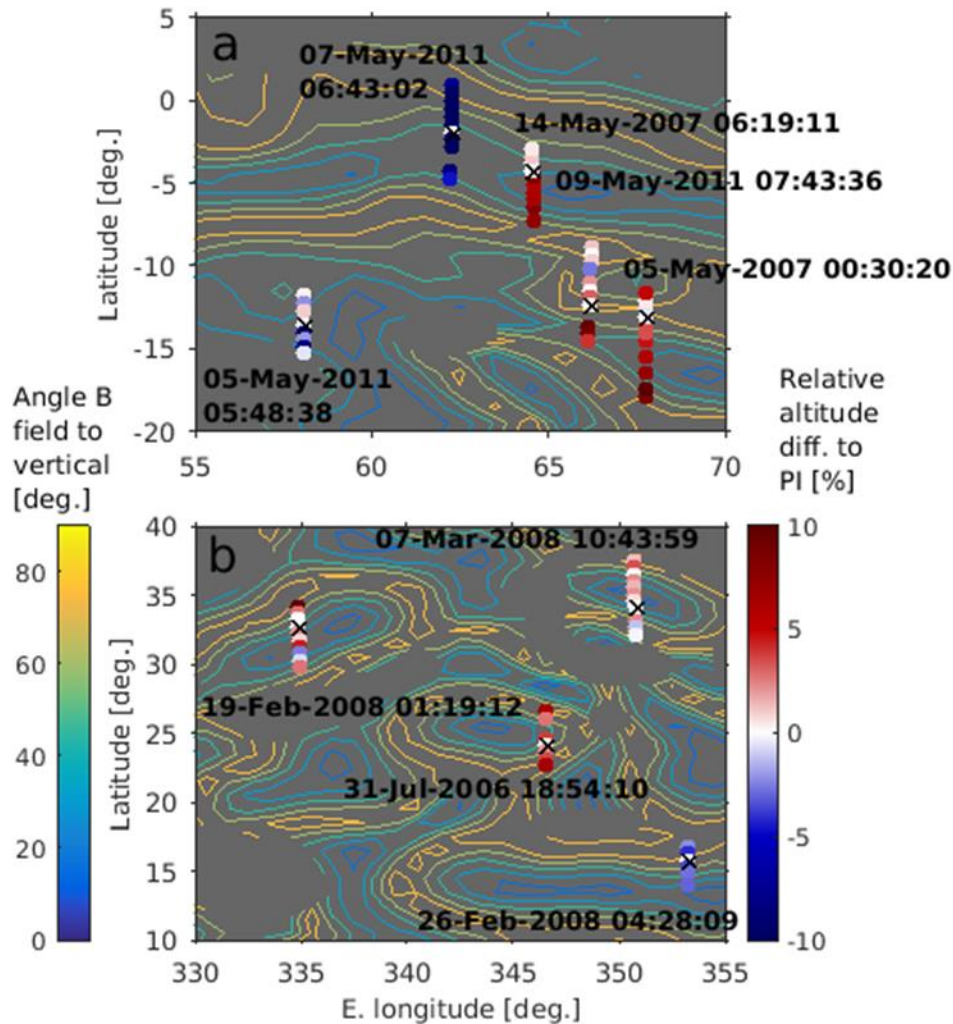1182   frequency levels within in the sensitivity gaps are not displayed to avoid a bias.
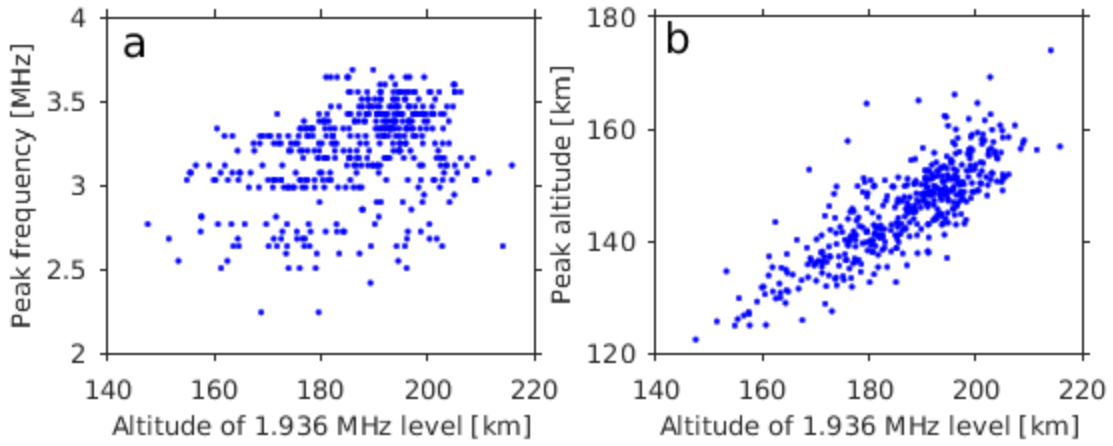
1183

Figure 10: Scatter plot of the altitude level at a fixed frequency 1.936 MHz versus the
ionospheric peak frequency (panel a) and versus the ionospheric peak altitude (panel b).

1184

1185

1186

1187

Figure 11: Maps showing regions of moderate crustal field strengths near the equator, in the
Southern hemisphere (panel a) and Northern hemisphere (panel b). These are maps of the angle
of the crustal magnetic field to the vertical from the model of Cain et al. (2003) evaluated at 150
km altitude, represented as color coded contours from 15 to 75° per step of 15° (going from near
horizontal to near vertical), using the colorbar on the left side. Fields of strength < 30 nT are
ignored. The footprint of MEX at the times of available EDPs of the time series of the individual
events observed in these regions are superposed onto the maps, colored for each event by the
altitude differences between the PI EDP and the other EDPs relative to the altitude of the PI EDP

1196 (in %), all taken at a fixed frequency 1.936 MHz. Negative altitude differences are colored in

1197 blue, zero differences in white and positive differences in red, using the colorbar on the right

1198 side. The date and time of the PI EDP are written next to each event, and its location marked by a

1199 black 'x'.

1200
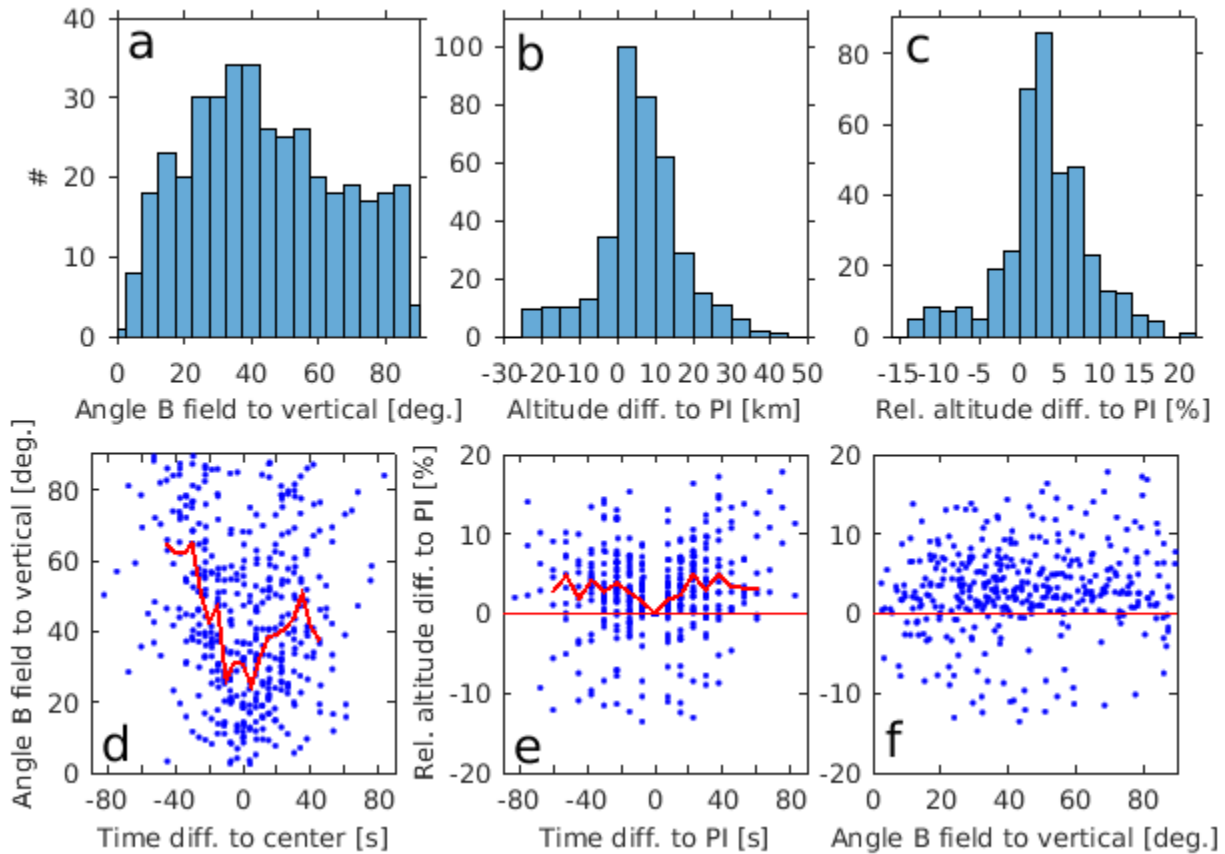
1201

1202 Figure 12: In this figure, the data points correspond to the altitude level at a fixed frequency

1203 1.936 MHz of all the available EDPs of the time series of all the events. (a) Distribution of the

1204 angle of the crustal magnetic field to the vertical. (b) Distribution of the altitude differences

1205 between the PI EDP and the other EDPs of the time series per event. (c) Distribution of the

1206 altitude differences between the PI EDP and the other EDPs of the time series, relative to the

1207   altitude of the PI EDP (in %), per event. (d) Superposed epoch analysis of the angle of the crustal

1208   field to the vertical, using the time difference in seconds compared to the center time of the

1209   density structure (which is centered at 0 s). Negative times are before the center time and

1210   positive times are after. The red line indicates the median values as a function of superposed

1211   epoch time. (e) Superposed epoch analysis of the relative altitude differences, using the time

1212   difference in seconds compared to the PI EDP time (which is centered at 0 s). Negative times are

1213   before the PI EDP time and positive times are after. The red line indicates the median values as a

1214   function of superposed epoch time. (f) Scatter plot of the angle of the crustal field to the vertical

1215   versus the relative altitude differences.

1216
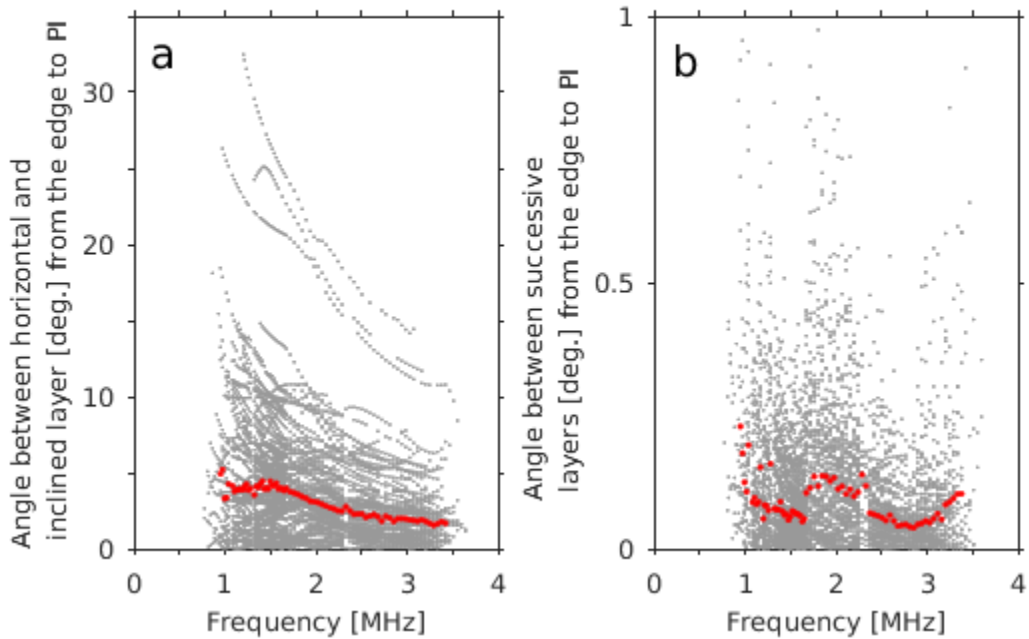
1218   Figure A1: (a) Distribution of the angle between the horizontal and the inclined layer from the

1219   edge point to the PI point, versus frequency, for all the events, for both the beginning and end

edges, plotted as grey dots. (b) Distribution of the angle between successive inclined layers (of consecutive frequencies), versus frequency, for all the events, plotted as grey dots. In both panels, the angles are shown in absolute value; the red dots indicate the median values versus frequency.